

# Bioinspired Rigid-Soft Hybrid Origami Actuator With Controllable Versatile Motion and Variable Stiffness

Zhuang Zhang , *Member, IEEE*, Genliang Chen , *Member, IEEE*, Yuanhao Xun, Yongzhou Long , Jue Wang , *Student Member, IEEE*, Hao Wang, and Jorge Angeles , *Fellow, IEEE*

**Abstract**—Conventional soft pneumatic actuators (SPAs) are made of soft materials that facilitate safe interaction and adaptability. In positioning and loading tasks, however, SPAs demonstrate limited performance. In this article, we extend the current designs of SPAs upon integrating a tendon-driven parallel mechanism into a pneumatic origami chamber, inspired by the performances and structures of vertebrates. The inner rigid/outer soft actuator exploits the advantages of both, parallel mechanisms to achieve precise, versatile motion, and SPAs, to form a compliant, modular structure. With the antagonistic actuation of tendons-pulling and air-pushing, the actuator can exhibit multimode motion, tunable stiffness, and load-carrying maneuvers. Kinematic and quasi-static models are developed to predict the behavior and to control the actuator. Using readily accessible materials and fabrication methods, a prototype was built, on which validation experiments were conducted. The results prove the effectiveness of the model, and demonstrate the motion and stiffness characteristics of the actuator. The design strategy and comprehensive guidelines should expand the capabilities of soft robots for wider applications, and facilitate the development of robots with rigid-soft hybrid structures.

**Index Terms**—Origami robots, parallel robots, soft robot materials and design, Soft sensors and actuators.

Manuscript received 15 May 2023; revised 26 July 2023; accepted 25 August 2023. This paper was recommended for publication by Associate Editor P. Renaud and Editor A. Menciassi upon evaluation of the reviewers' comments. This work was supported in part by the National Key Research and Development Program of China under Grant 2019YFA0709001 and in part by the Natural Science Foundation of China under Grant 52205031 and Grant 52022056. This video shows the design and behavior tests of the proposed actuator. (*Corresponding authors: Genliang Chen; Zhuang Zhang.*)

Zhuang Zhang is with the State Key Laboratory of Mechanical System and Vibration, and Shanghai Key Laboratory of Digital Manufacture for Thin-walled Structures, Shanghai Jiao Tong University, Shanghai 200240, China, and also with the School of Engineering, Westlake University, Hangzhou 310030, China (e-mail: zhangzhuang@westlake.edu.cn).

Genliang Chen is with the Meta Robotics Institute, and the State Key Laboratory of Mechanical System and Vibration, Shanghai Jiao Tong University, Shanghai 200240, China (e-mail: leungchan@sjtu.edu.cn).

Yuanhao Xun, Yongzhou Long, Jue Wang, and Hao Wang are with the State Key Laboratory of Mechanical System and Vibration, and Shanghai Key Laboratory of Digital Manufacture for Thin-walled Structures, Shanghai Jiao Tong University, Shanghai 200240, China (e-mail: 1056411499@qq.com; yzlong@sjtu.edu.cn; wang5056@purdue.edu; wanghao@sjtu.edu.cn).

Jorge Angeles is with the Department of Mechanical Engineering and the Centre for Intelligent Machines, McGill University, Montreal, QC H3A 0G4, Canada (e-mail: angeles@cim.mcgill.ca).

This article has supplementary material provided by the authors and color versions of one or more figures available at <https://doi.org/10.1109/TRO.2023.3311630>.

Digital Object Identifier 10.1109/TRO.2023.3311630

## I. INTRODUCTION

INSPIRED by the softness and natural compliance of biological systems, soft pneumatic actuators (SPAs) have been widely explored and applied in the field of robotics and human-robot interaction [1], [2], [3]. As opposed to conventional rigid actuators, their soft counterparts have bodies made out of intrinsically deformable materials, whose elastic moduli are comparable with those of natural organisms, while exhibiting a number of passive degrees of freedom (DoF). Correspondingly, the passive compliance generated by flexible materials and compressed air, provides more sensitive, reliable protection, independent of the control algorithm [4], [5], [6].

Over the years, soft robotic designs that employ structures similar to cephalopods have been proposed [7], [8], [9], [10], [11], [12], [13], [14], [15], [16], [17]. These actuators contain no endoskeleton and consist entirely of elastomers like silicon rubbers. Analogous to the working principle of animal ligaments, elastomers can realize actions such as extension, bending, and twisting, when pressurized through the embedded pneumatic channels, while rebounding passively when depressurized. Such deformation-induced motion is dexterous and safe for interaction with the environment. However, their performance deteriorates when a high payload is required, due to their intrinsically flexible, isotropic structures. Moreover, the large deformation of elastomers leads to nonlinear characteristics, which makes accurate position and motion control of soft actuators still a challenge [18]. Entirely soft structures and their infinite dof render the control much harder upon loading.

SPAs with rigid elements have been proposed to expand their capabilities [19], [20]. Such hybrid structures can contribute to enhancing their load-carrying capacity and better control their motion [21]. Rigid shells [22] and frames [23] have been proposed to constrain the deformation of the elastic pneumatic chambers. The soft chambers are thus protected, and their motion types confined. Nevertheless, few attempts have been reported to enhance their positioning accuracy or simplify the motion control, upon integrating additional rigid elements. Origami robots, whose morphology and function are generated by folding, have drawn increasing attention in recent years [24], [25], [26], [27], [28], [29], [30], [31], [32]. The integration of origami structures into SPAs has been shown to enhance their off-axis stiffness [33]. The load-carrying capacity of SPAs with origami

structures has been improved accordingly; even vertical weight-lifting tasks can be realized [34], [35]. Furthermore, due to their reconfigurable structures, origami chambers can be actuated under lower pressure, and their motion regulated with a higher extension/contraction ratio [35], [36], [37], [38], [39], [40], [41]. However, most existing designs utilize simple, hollow chamber structures, which typically exhibit prescribed, unimodal motion upon inflation. The nonlinear relationship between pneumatic pressure and elastic deformation renders accurate open-loop motion control still challenging and highly dependent on the payload.

It is worth noting that many animals, such as mammals, birds, and fish, possess bones or cartilages inside their bodies. Accurate, powerful motion can be achieved with rigid skeletons, while soft muscles and tissue provide compliant interaction. Recently, several concepts have been proposed to integrate rigid endoskeletons into soft bodies to form hybrid structures [42], [43], [44], [45]. Among these designs, most of the rigid components are connected in series to form passive, hyper-redundant endoskeletons. The rigid skeletons constrain the motions of the soft chambers and reduce the passive deformation in undesirable directions. The stiffness in specific directions is accordingly enhanced, so that the load-carrying capacity can be readily improved. However, since most rigid components are serially connected through revolute joints that are confined to the same plane, only single-mode, unidirectional bending can be realized. Moreover, the capability of extension/contraction is restricted, which unavoidably reduces the dexterity and functionality of the actuator. In addition, passive hyper-redundant endoskeletons contain a large number of passive dof. Accurate motion control will still be hard to achieve, due to the nonlinearities involved, especially in the presence of a payload [46], [47], [48].

Here, we report the design, fabrication, modeling, and performance of a rigid-soft hybrid actuator, aiming at the weaknesses of SPAs in accurate multimode motion control and load carrying. Through integrating a tendon-driven rigid parallel mechanism into a pneumatically driven soft origami chamber, the proposed actuator forms an inner rigid/outer soft hybrid structure, similar to vertebrates. The motion of the origami chamber is thus confined by the parallel mechanism in a fully controllable three-dof workspace, including extension, contraction, omnidirectional bending, and circular swing. Accordingly, the intrinsically compliant actuator can achieve accurate motion control dispensing with complicated analysis of nonlinear deformation, since the kinematics of the inner mechanism can be expressed in a simple, symbolic form. The tendons inside the mechanism and the air inside the origami chamber form an antagonistic actuation system, rendering the actuator to perform bidirectional output force and tunable stiffness. Benefitting from the antagonistic actuation system and the hybrid structure, the actuator can execute weight-lifting maneuvers when loaded with tenfold its weight, a challenge for most soft robotic actuators. In addition, the foldable, rigid-soft hybrid design principle leads to several merits, including low cost, simple-to-fabricate, high extension ratio, low demand of input pressure, and no radial expansion.

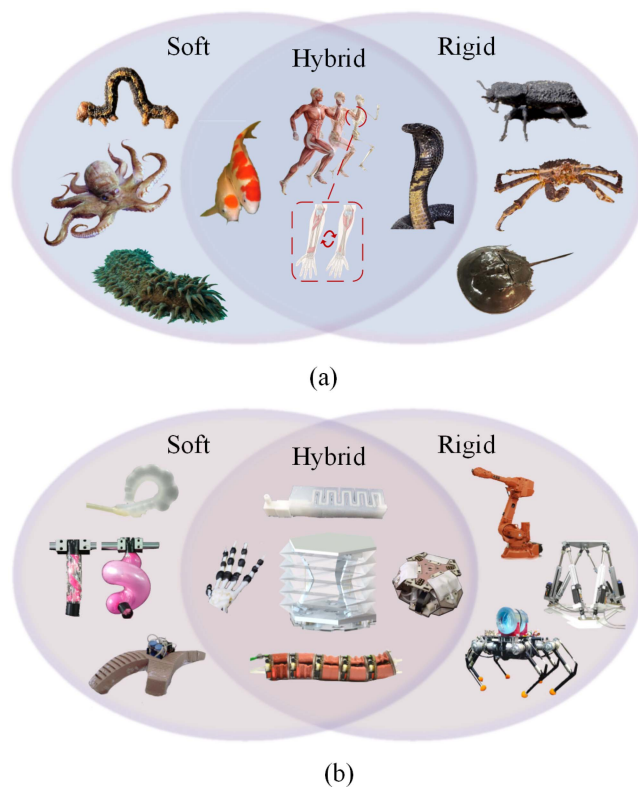


Fig. 1. Bioinspiration from vertebrates and its implementation in robotics. (a) Invertebrates are either entirely soft or inner soft/outer rigid. In contrast, vertebrates possess inner rigid/outer soft hybrid structures. (b) Most robots exhibit either entirely soft or rigid structures, just like invertebrates. Inspired by vertebrates, our design has an inner rigid/outer soft hybrid structure. The images of the prototypes are reproduced with permission from the authors.

The rest of the article is organized as follows. In Section II, the bioinspiration concept is introduced, along with the particular implementation of the rigid-soft hybrid actuator from the perspective of both structure and actuation. This is followed in Section III by a detailed description of the mechanical design, as well as the fabrication method. Section IV includes the models that characterize the kinematic and quasi-static behavior of the actuator. The performance of the actuator, validation of the design principle and the models, besides the multimode behavior are introduced in Section V. Finally, Section VI concludes this article.

## II. BIOINSPIRATION AND IMPLEMENTATION

### A. Bioinspiration of the Rigid-Soft Hybrid Structure

Broadly speaking, animals can be divided into two categories, invertebrates and vertebrates [49]. Invertebrates account for more than 90% of the world's animals, which include cephalopods, arthropods, echinoderms, etc. These animals either are entirely soft or carry rigid exoskeletons, as shown in Fig. 1(a). The soft ones achieve more friendly interactions with the environment. However, their soft structures are relatively weak in body-supporting [50]; the capability of stiffening is essential for load-carrying motions [51]. On the contrary, although more or less compliant parts exist in their bodies, the rigid ones

with exoskeletons exhibit high stiffness to environmental impact due to their tough armors, just like what ironclad beetles have demonstrated [52]. Their motions can be accurate and powerful; nevertheless, it is apparent that compliant, safe interactions with them pose tough challenges.

Compared with invertebrates, vertebrates, like humans, carry more advanced structures that can be regarded as combinations of soft and rigid components. As shown in the bubble intersection of Fig. 1(b), vertebrates have rigid skeletons that are wrapped in soft muscles. Rigid skeletons ensure motion accuracy and maintain the body structure, while soft muscles actuate skeletons and provide soft interactions. In this way, the inner rigid/outer soft hybrid structure can execute accurate, powerful motions, while maintaining the safety of interactions. It is noteworthy that not all the skeletons of vertebrates are connected in series. There are also some skeletons in parallel structures that can perform more versatile motion types, e.g., the ulna and the radius in human arms or some bird wings, as depicted in the bubble intersection of Fig. 1(a).

Inspired by the hybrid structures of vertebrates, we propose an origami actuator with a hybrid structure, as well as a hybrid actuation system. As shown in Fig. 1(b), most soft and commercial robots exhibit either entirely soft or entirely rigid structures, similar to invertebrates. On the contrary, in our design, a rigid tendon-driven parallel mechanism is wrapped in a soft pneumatic origami chamber, which has a design principle similar to that of human arms and is distinct from other novel hybrid designs that possess serially connected endoskeletons inside rubbery chambers [42], [43], [44], [45], hollow origami structures [30], [53], [54], [55], [56], and distributed rigid-soft structures [31], [33], [57], [58], [59]. The parallel mechanism functions as a rigid skeleton inside the body of a vertebrate, while the tendon and the pneumatic pressure work antagonistically like muscle pairs arranged around bones, resulting in a different structure and control logic with existing designs of pneumatic/tendon-driven hybrid actuators [60], [61], [62]. Consequently, the hybrid origami actuator can simultaneously realize simply-controlled accurate motions, soft interactions, load carrying, and variable stiffness, in principle.

### B. Concept of the Rigid-Soft Hybrid Actuator

As shown in Fig. 2(a), the proposed actuator mainly consists of a pneumatically driven soft origami chamber and a tendon-driven rigid parallel endoskeleton. The origami chamber comprises discrete, rigid, thin panels, and smooth folds. The inflation of the chamber is confined by the origami without losing compliance, besides being suitable for extension, contraction, and omnidirectional bending. The endoskeleton consists of rigid links with flexible joints, and forms a foldable parallel mechanism. The totally passive flexible joints ensure the compliance of the endoskeleton, while the motion of the moving platform is constrained to three-dof, as opposed to infinitely many dof of most SPAs.

The origami chamber [see Fig. 2(b)] forms a sealed cylindrical soft structure so that it undergoes extension when inflated, contraction when deflated. Consisting of rigid panels and

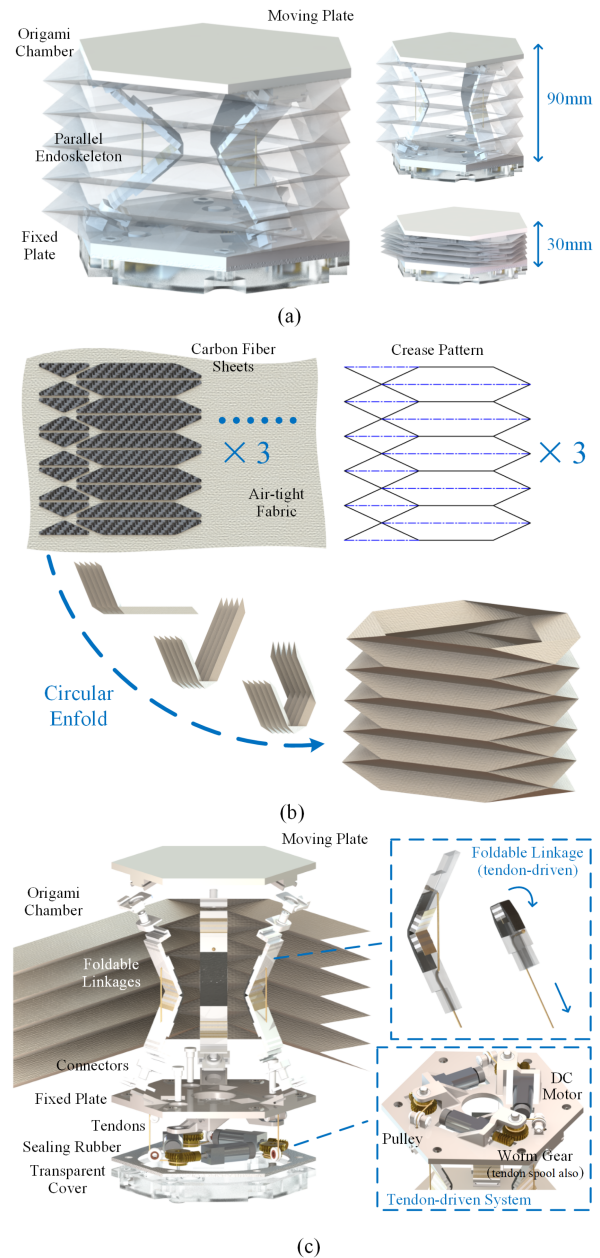


Fig. 2. Concept of the bioinspired rigid-soft hybrid origami actuator. (a) Structure of the actuator. The actuator can be divided into two parts, the soft origami chamber and the rigid parallel endoskeleton. (b) Structure of the origami chamber. The 0.6-mm carbon fiber sheets are discretely pasted up on a piece of air-tight fabric based on the Yoshimura pattern, with a 2-mm gap between each two sheets. (c) Structure of the parallel endoskeleton. Three foldable linkages with identical structures form a foldable 3-URU parallel mechanism, together with the moving and fixed plate. The pneumatic actuation system is off-board and inflates the origami chambers through silicon tubes connected with the transparent cover.

fabric-based, unstretchable folds, the chamber produces negligible elastic deformation, thus having low demand of actuation pressure. However, the simplified structure is also accompanied by control problems. The positive pressure can be regarded as a one-way actuation, to some extent. Since neither predesigned pneumatic channels nor elastic deformation exist, the motion of the origami chamber cannot be controlled by means of pressure,

unlike most SPAs made of elastomers. The chamber can achieve no prescribed motion trajectory but simply extend when inflated, except for passive deformation caused by an external force. Hence, controllable elements are indispensable to solve and simplify the control issues.

The endoskeleton [see Fig. 2(c)] comprises three limbs and shares the same base and moving platforms with the origami chamber. This system can thus be regarded as a 3-URU parallel mechanism with flexible joints. The parallel endoskeleton possesses three-dof and is axially foldable, which can work together with the cylindrical origami chamber and constrain the motion of the moving platform. Unlike conventional rigid parallel mechanisms, neither bulky motors nor pneumatic cylinders are directly connected to the joints. Instead, three tendons are inserted into the three foldable linkages, intended to constrain the rotations of the flexible joints. The motion of the moving platform is thus geometrically confined by the lengths of the tendons. Similar to positive pressure, tendon-driven actuation is also a one-way actuation system that can only constrain the joint rotation in one direction (tendon tension). Therefore, the moving platform is still structurally compliant, capable of producing passive bending and contraction, although the passive deformation is constrained to a three-dof workspace.

From the viewpoint of the structure, both the origami chamber and the parallel endoskeleton are versatile mechanisms that can achieve extension, contraction, and omnidirectional bending. The origami exhibits structural compliance because of its reconfigurable structure; however, such a feature is also accompanied by control problems. In contrast, the three-dof motion of the parallel endoskeleton is fully constrained by the three tendons; however, the multilink structures exhibit lower compliance and cannot form sealed modules, rendering them less interactive and hard to operate as modular actuators. Consequently, a proper combination of the soft origami chamber and the rigid parallel endoskeleton can integrate the merits, while avoiding the weaknesses of both origami chambers and parallel mechanisms. The proposed rigid-soft hybrid actuator is modular and compliant, by virtue of the integration of the pneumatic origami chamber. The sealed chamber protects the tendons from environmental interference, thus ensuring the geometric constraints. Correspondingly, such a hybrid system makes the versatile motion fully controllable. The control strategy is also simplified, since the kinematics of the whole actuator lies on the tendon-constrained parallel mechanism, which can be expressed in symbolic form.

From the viewpoint of the actuation, the two one-way actuation sources act antagonistically on the moving platform (tendon-pulling, air-pushing). Hence, a hybrid actuation system that can simultaneously control the stiffness and the motion of the actuator is obtained. The tendons will produce tension because of the antagonistic force provided by the air pressure. In this way, fairly accurate motion control can be achieved by the tendon-driven system, together with the parallel endoskeleton. Besides, tuning the pressure inside the chamber will lead to a variation of the internal force; the stiffness can be accordingly adjusted. Variable stiffness is a key factor for compliant, deformable structures to enhance their load-carrying capacity [3], [51]. Therefore, the proposed design theoretically ensures both

the positioning and the load-carrying capacity of the actuator. Moreover, since the input pressure has no correlation with the endoskeleton confined by the tendon-driven system, the stiffness of the actuator can be adjusted actively and stepwise at any configuration.

### III. DESIGN AND FABRICATION

#### A. Design of the Origami Chamber

The origami chamber is the core actuation component to achieve the stiffness variation, and determine the load-carrying capacity of the actuator. The expected three-dof motion requires the chamber to exhibit omnidirectional bending and extension/contraction capabilities. Besides, aiming at the common weakness of other SPAs, the desirable features of the origami chamber include: large extension/contraction ratio; no radial expansion; low threshold pressure; and ease of fabrication. The Yoshimura pattern [63] is a cylindrical folding origami that has been reportedly used to design soft linear actuators [34], [64], [65]. However, this pattern is actually a solid structure and is discontinuously foldable [66]. Most existing designs employ low-stiffness shells like laser-machined paper sheets [33], [64] or polymers (e.g., PET) [54], [67] to build Yoshimura structures. The low-stiffness shells can be readily deformed during the folding process. The contraction ratios are accordingly improved; even omnidirectional bending can be realized. However, the hollow origami chamber in our design requires positive pressure; these low-stiffness shells are readily inflated into a right cylinder when pressurized. Moreover, small holes are inevitable on laser-machined origami shells, which will lead to serious air leakage.

To alleviate the aforementioned shortcomings, a rigid-soft hybrid Yoshimura origami chamber, consisting of air-tight fabric and carbon fiber sheets, is designed as described here. Shown in Fig. 2(b) are the 0.6-mm carbon fiber sheets pasted up on a piece of fabric, in accordance with the Yoshimura base-crease pattern, with a 2-mm gap between each two sheets. Due to the precise soft gaps between the rigid sheets, the proposed 3-D origami chamber can be formed by means of a simple circular enfolding of the 2-D piece. Complex and time-consuming manual folding is thus avoided, unlike existing designs of origami structures. The carbon fiber sheets will keep rigid during the folding process of the chamber. The 2-mm fabric gaps form smooth folds to connect the rigid panels, as well as to ensure the folding process (extension/contraction) and the passive bending deformation. In this way, the radial expansion will be effectively avoided during the motion process, due to the unstretchable fabric and the high-stiffness sheets. Fig. A1, given in the Supplementary Material, shows comparisons between the proposed rigid-soft hybrid chamber and its common low-stiffness counterpart made of thick paper. It is shown that the hybrid chamber performs better in holding its structure when pressurized. In addition, since almost no elastic deformation exists and no commonly used elastomer (e.g., silicon rubber) is utilized, the hybrid chamber will be readily inflated, while exhibiting an extremely low threshold pressure.

### B. Design of the Tendon-Driven Parallel Endoskeleton

The tendon-driven parallel endoskeleton is mainly designed to accurately control the configuration of the moving platform, and produce antagonistic actuation together with the positive pressure. As shown in Fig. 2(c), the endoskeleton carries three equally spaced foldable linkages that connect the base and the moving platforms. Each linkage consists of two rigid panels with the same geometric parameters and five revolute joints. The axes of rotation of the first two joints intersect at right angles, thereby forming a universal joint. The last two joints are similarly arranged so that the endoskeleton can be regarded as a parallel mechanism with a 3-URU topology. Then, the mobility of the moving plate can be calculated as

$$F = \lambda(n - j - 1) + \sum_i f_i$$

$$= 6 \times (8 - 9 - 1) + 6 \times 2 + 3 \times 1 = 3 \quad (1)$$

where  $\lambda = 6$  accounts for the dof of a rigid body in space, while  $n$  and  $j$ , the numbers of links and joints, respectively. As well,  $f_i$  denotes the dof associated with the  $i$ th joint.

Apart from the omnidirectional bending, the three-dof endoskeleton can also achieve vertical translation, which ensures the folding capability of the whole actuator. Furthermore, 4-mm panels are used as rigid links in order to improve the folding range (i.e., the contraction ratio). Instead of conventional rigid hinges, soft, but unstretchable fabric pieces are utilized to form flexible hinges between the rigid panels, which simplifies the fabrication, enhances the folding capability, and makes the skeleton more compliant. In this way, the rigid-soft hybrid linkages possess foldable structures similar to those of the origami chamber, consisting of rigid thin panels and smooth folds. In addition, silicon rubber panels are attached to the back of the revolute joints, providing additional elasticity to keep the tendons in tension. The initial configuration of the linkages is slightly folded to avoid partial singularities and ensure pretensions. Therefore, the actuator can perform controllable motion all the time, even in the absence of air supply when unloaded.

As shown in Fig. 2(c), the tendons are inserted into the lower links to confine the tendon routes, and make the structure more compact, inspired by the tendon-driven robotic hands. The two ends of each tendon are connected to the upper link and the worm-wheel roller, respectively. The length of the tendon is constant, except for the part between the upper and lower links so that the rotations of the revolute joints can be controlled by rolling the inserted tendons. Worm gears are designed to transmit the rotation from the micro dc motors to the rollers. Due to the self-locking characteristics of the worm gears, the structure, rather than the motors, will withstand the antagonistic force generated by the air pressure. Hence, micromotors with relatively low output torque can be utilized to form antagonistic actuation; the integration will benefit from the microstructures.

### C. Fabrication of the Origami Chamber

The origami chamber, consisting of discrete carbon fiber sheets and air-tight fabric coated with thermoplastic

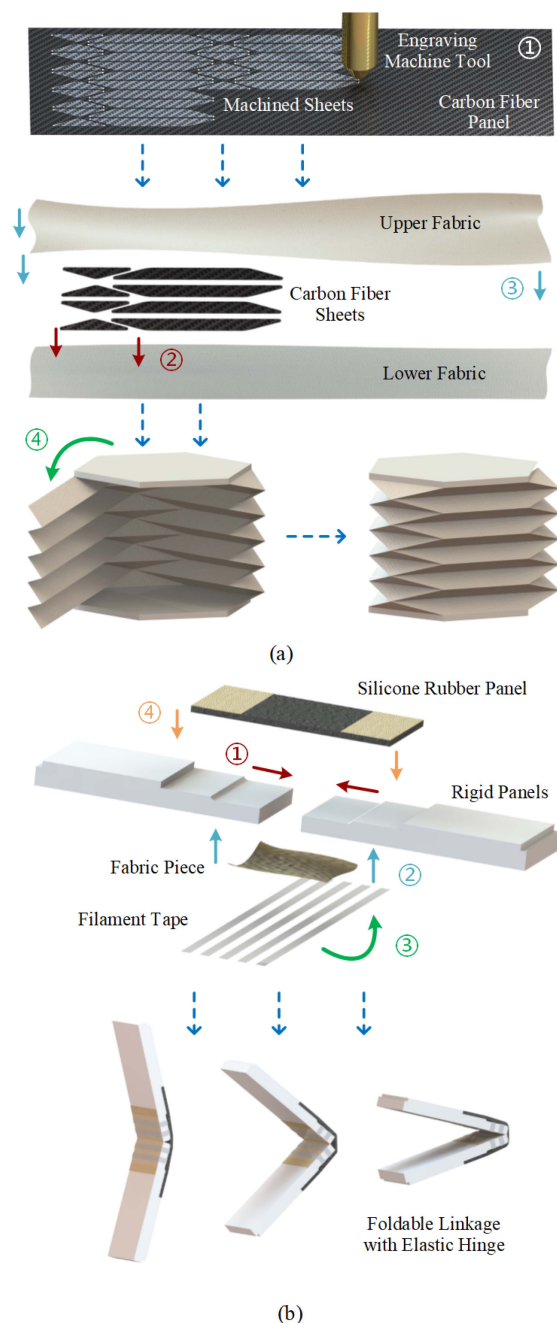


Fig. 3. Fabrication process. (a) Origami chamber. Step 1: Carbon fiber sheets cut, with an engraving machine; step 2: Paste the carbon fiber sheets onto the lower fabric; step 3: Paste another piece of fabric onto the sheets and paste the rims of two pieces of fabric together; and step 4: Roll the 2-D structure into a 3-D cylinder and paste onto the two plates. (b) Foldable linkage. Step 1: Connect two rigid panels; step 2: Seam the panels by pasting a piece of fabric; step 3: Wrap the filament tape around the seam and cut the side without fabric; and step 4: Paste a silicon rubber panel onto the connected panels.

polyurethane (TPU), can be obtained based on a layer-fabrication method, as shown in Fig. 3(a). The base structure is a rectangular 0.6-mm carbon fiber panel, whose two facets can be bonded with fabric tapes (Mileqi Adhesive). Cut by a 2-D engraving machine based on the crease pattern shown in Fig. 2(b), two kinds of sheets can be separated from the base structure. It is noteworthy that a mold should be pressed on the lower

fabric during the second step, in order to improve the fabrication accuracy. The discrete sheets are then manually placed into the mold and adhered to the fabric through the prebonded tape. A second piece of fabric is used to form a sandwich structure, to improve the stretch strength and air tightness, after removing the mold. Finally, wrapping the 2-D structure around the base and the moving platform, a 3-D origami chamber is obtained. The origami chamber, together with the fixed and moving plates, forms a closed structure via gluing (Instant Adhesive 5569, Kaibingtuan). The radial edges of the chamber can be sealed through stacking and pasted by soft fabric glue, making the whole system air tight. The formed hollow structure is relatively simple and simple-to-fabricate, without predesigned, complex pneumatic channels inside the chamber, unlike most SPAs made of silicon rubber.

#### D. Fabrication of the Tendon-Driven Parallel Endoskeleton

As described previously, the parallel endoskeleton has a hybrid structure consisting of rigid links and flexible hinges, similar to the origami chamber with rigid panels and smooth folds. The rigid links, together with the moving and base platforms, are 3-D printed. The flexible hinges are fabricated based on a new method, using unstretchable fabric pieces and stretchable silicon rubber panels. The fabrication process is illustrated in Fig. 3(b). Two rigid links are tied together by a piece of fabric on only one side of the links. Filament tape (Scotch 8915, 3 M) is wrapped around the hinge, and manually cut on the side free of fabric, in order to enhance the torsional stiffness of the flexible hinge. A 1-mm silicon rubber panel (Ecoflex 00-10) is pasted on the back of the hinge using silicon glue (Instant Adhesive 5562, Kaibingtuan). Two small fabric pieces can also be pasted upon the back of the silicon rubber and form an uncovered gap. These two pieces are used to adjust the partial stretchability of the silicon rubber; the uncovered gap is the only part that stretches with the rotation of the hinge. In this manner, the stretching of the silicon rubber can be tuned to provide little but sufficient elasticity to the flexible hinges, in order to keep the tendons under tension.

### IV. MODELING

#### A. Kinematics

The proposed endoskeleton that constrains the three-dof motion of the proposed actuator can be modeled as a 3-URU parallel mechanism with flexible joints. Thus, the inverse kinematics of the mechanism will contribute to the motion control of the actuator. This mechanism is a versatile type that exhibits various kinematic characteristics upon changing the arrangements of the universal joints [68]. However, current research on the kinematics of this type has mainly focused on the translational 3-URU (or 3-UPU) and 3-URU wrists that generate three translations (3T) and three rotations (3R) motions, respectively [69], [70]. Few works have reported on the analysis of the 3-URU mechanism with 1T2R (one translational and two rotational) motion. In this section, the kinematics of the proposed 3-URU endoskeleton with 1T2R motion is analyzed. Note that the axes of the first and

the fifth revolute joints (inside the universal joints) of each limb should be neither parallel nor intersected at the rotation center of the platform, to enable such kind of motion.

Schematics of the endoskeleton are illustrated in Fig. 4. The base and the moving platforms (i.e., platforms  $A_1A_2A_3$  and  $C_1C_2C_3$ ) bear the same geometric parameters, and are mutually parallel at the initial posture, as depicted in Fig. 4(a). The lengths of the two links in each limb are identical. The angle between the moving platform and the upper universal joint is identical to that between the base platform and the lower universal joint. Thus, the parallel mechanism (namely, the endoskeleton) carries a symmetric structure. For kinematics modeling, two reference frames, the spatial  $\{S\}$  and its tool counterpart  $\{T\}$ , are constructed at the centers of the base and the moving platforms, respectively.

As stated previously, the proposed parallel mechanism can generate 1T2R motion, including contraction/extension and omnidirectional bending. The latter can be regarded as a rotation around any radial direction stemming from a given point, with no rotation around the  $z$ -axis. In order to describe the three-dof motion, a set of variables is introduced. Three generalized coordinates,  $\alpha$ ,  $\beta$ , and  $h$ , are defined as shown in Fig. 4(b). Here,  $\alpha$  denotes the angle between the  $x$ -axis and the projection of the  $z'$ -axis on the  $Oxy$ -plane;  $\beta$  denotes the angle between the  $z'$ -axis and the  $z$ -axis;  $h$  represents the distance between the centers of the base and that of the moving platforms, namely  $O$  and  $O'$ . The radial bending direction is represented by  $\alpha$ . The posture of the moving platform can be obtained by a rotation around an axis perpendicular to the  $z$ -axis, according to Euler's rotation theorem. Thus, the axis of rotation  $e$ , with respect to the spatial frame  $\{S\}$ , can be expressed as

$$e = \left[ \cos\left(\alpha - \frac{\pi}{2}\right), \sin\left(\alpha - \frac{\pi}{2}\right), 0 \right]^T. \quad (2)$$

Then, the rotation matrix that represents the posture of the moving platform can be derived based on the product-of-exponential formula [71], [72] as follows:

$$\mathbf{R} = \exp(\hat{e}(-\beta)) = \mathbf{I} + \sin(-\beta)\hat{e} + (1 - \cos(-\beta))\hat{e}^2 \quad (3)$$

where  $\mathbf{R} \in SO(3)$ ; and  $\mathbf{I} \in \mathbb{R}^{3 \times 3}$  is the  $3 \times 3$  identity matrix.

Since all the links bear the same lengths, it is apparent that the mechanism architecture is symmetric with respect to the plane of the centers of the three revolute joints,  $B_1$ ,  $B_2$ , and  $B_3$ . The intersection of the  $z'$ -axis with the  $z$ -axis, labeled  $B_O$ , is also located in this plane because of the symmetry. As a consequence,  $\triangle OB_OO'$  is an isosceles triangle, as the lengths of its two sides are equal (i.e.,  $l_{OB_O} = l_{O'B_O}$ ). Moreover, the base angle of  $\triangle OB_OO'$  satisfies

$$\gamma = \angle B_OOO' = \frac{\beta}{2}. \quad (4)$$

Then, the position of the moving platform (given by point  $O'$ ), in the spatial frame  $\{S\}$ , can be expressed as

$$p_{O'} = \left[ h \sin \frac{\beta}{2} \cos \alpha, h \sin \frac{\beta}{2} \sin \alpha, h \cos \frac{\beta}{2} \right]^T. \quad (5)$$

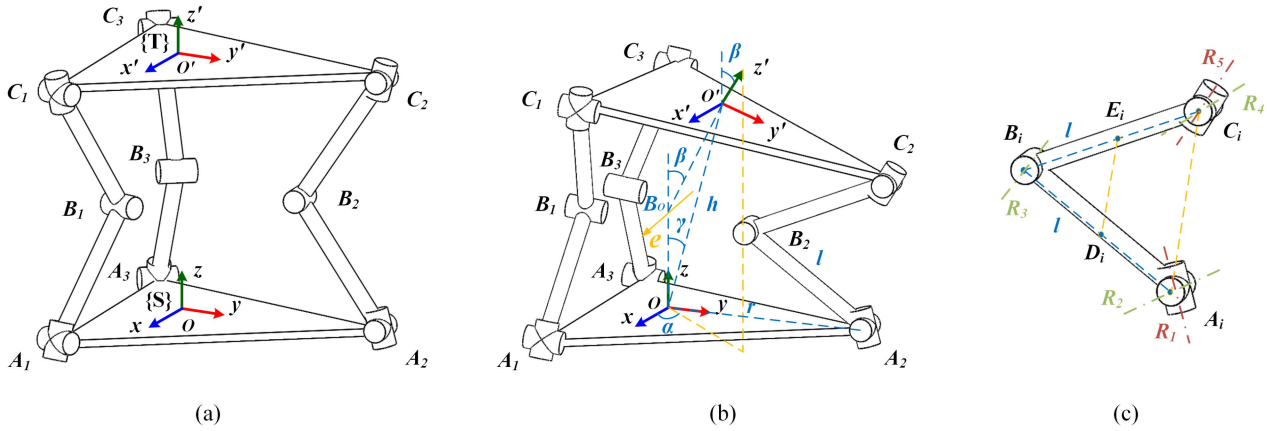


Fig. 4. Schematics of the endoskeleton. (a) Initial configuration. (b) Bending around a specific direction. (c) Single foldable limb consisting of two rigid links with the same length  $l$  and five revolute joints  $R_1 - R_5$ . In the kinematic model, three parameters:  $\alpha$  (the angle between the  $x$ -axis and the projection of the  $z'$ -axis on the  $Oxy$ -plane);  $\beta$  (the angle between the  $z'$ -axis and the  $z$ -axis); and  $h$  (the distance between the center of the base and that of the moving platform) are the generalized coordinates.

The coordinates of the joints on the moving platform, in the spatial frame  $\{S\}$ , can then be expressed as

$$\mathbf{p}_S = \mathbf{R} \mathbf{p}_T + \mathbf{p}_O \quad (6)$$

where  $\mathbf{p}_S$  denotes the coordinates in the spatial frame  $\{S\}$ , while  $\mathbf{p}_T$  the coordinates in the tool frame  $\{T\}$ .

Moreover, the coordinates of  $C_1, C_2$ , and  $C_3$  in the tool frame  $\{T\}$ , as well as the coordinates of  $A_1, A_2$ , and  $A_3$  in the spatial frame  $\{S\}$ , are displayed as follows:

$$\begin{aligned} \mathbf{p}_{T, C_1} = \mathbf{p}_{S, A_1} &= \left[ \frac{\sqrt{3}}{2}r, -\frac{1}{2}r, 0 \right]^T \\ \mathbf{p}_{T, C_2} = \mathbf{p}_{S, A_2} &= [0, r, 0]^T \\ \mathbf{p}_{T, C_3} = \mathbf{p}_{S, A_3} &= \left[ -\frac{\sqrt{3}}{2}r, -\frac{1}{2}r, 0 \right]^T \end{aligned} \quad (7)$$

where  $r$  denotes the radius of the circumscribing circle of either the base or the moving platform.

Then, the distance between two universal joints in each limb is

$$l_{A_i C_i} = \|\mathbf{p}_{S, C_i} - \mathbf{p}_{S, A_i}\|, \quad i = 1, 2, 3. \quad (8)$$

The angles that represent the rotations of the three revolute joints can then be expressed as

$$\phi_{B_i} = \arccos \left( \frac{2l^2 - l_{A_i C_i}^2}{2l^2} \right), \quad i = 1, 2, 3 \quad (9)$$

where  $l$  is the link length.

It is noteworthy that the three tendons are used to control the rotations of the three revolute joints. As shown in Fig. 4(c), the two ends of the tendon are located at the middle point of each link. Therefore, the length of the tendon can be derived as

$$l_{D_i E_i} = \frac{\|\mathbf{p}_{S, C_i} - \mathbf{p}_{S, A_i}\|}{2}, \quad i = 1, 2, 3. \quad (10)$$

In this way, the relation between the tendon length and the configuration of the moving platform is obtained, then applied to the motion control of the proposed actuator.

### B. Quasi-Statics

The quasi-static analysis leads to the relations between the output force and the input pressure, under different actuator configurations. Such relations are crucial in controlling the input pressure, as needed to realize weight-lifting tasks and tune the stiffness appropriately. The weight-lifting tasks mainly refer to a pushing-up process, rarely achieved by most soft robotic actuators. Benefitting from the antagonistic actuation system, the thrust force generated by the pneumatic pressure, can prompt the actuator to achieve pushing up tasks. In this section, the thrust force generated by the input pressure of the origami chamber, rather than the thrust force generated by the elastic rubber panels (antistretching) and the tensile force generated by the tendons, is analyzed since the latter two contribute little to force output. Accordingly, the analysis considers only the linear deformation of the origami chamber, since the weight-lifting task is mainly a translational process; the Yoshimura pattern deforms more regularly during this motion. Further, it should be noted that the crease  $DE$  shown in Fig. 5(a), namely, the longest valley crease of the base crease pattern, is assumed to be length changeable, to solve the nonrigid foldable problem of the Yoshimura pattern, which is in accordance with the deformable 2-mm-width folding crease of the rigid-soft hybrid origami chamber. Then, other creases can exhibit constant lengths during the deformation process. Two constants,  $a$  and  $\theta$ , which denote the length of the creases,  $AB$  and  $BC$ , and the base angle of the isosceles triangle  $ABD$ , are given as known parameters.

As for the quasi-static model, the principle of virtual work is utilized to build the relation among the output force, the input pressure, and the deployment height of the origami chamber. The relation can be expressed as

$$F = -P \frac{dV}{dh} \quad (11)$$

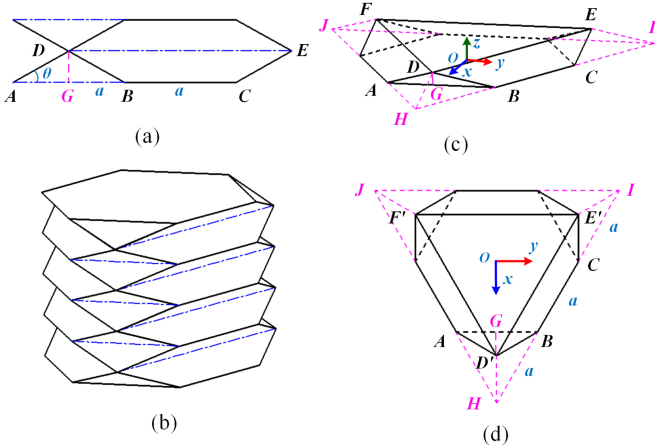


Fig. 5. Schematics of the origami chamber. (a) 2-D base crease pattern unit with two known geometric parameters; solid lines represent mountain creases; dash dot lines represent valley creases. (b) 3-D origami pattern after folding. (c) Half layer of the 3-D pattern; three triangular pyramids drawn in dash lines are added to form a regular pentahedron. (d) Top view of the half layer.

where  $F$  denotes the output force.  $P$  is the input pressure, while  $dh$  and  $dV$  represent the small changes of the deployment height and the internal volume of the origami chamber.

As shown in Fig. 5(b), the Yoshimura origami pattern carries a multilayer symmetrical structure; the origami chamber is assumed to be evenly deployed during the morphing process. Hence, a half layer is used to analyze the relationship between volume and height, in order to simplify the derivation process, as depicted in Fig. 5(c). Since the half layer is an irregular octahedron, three triangular pyramids are added to form a regular solid, namely, a pentahedron. Then, the volume of the half-layer chamber can be represented as the volume of the regular pentahedron subtracting the volume of three triangular pyramids, and can be written as

$$V = V_p - 3V_t \quad (12)$$

where  $V_p$  represents the volume of the regular pentahedron

$$V_p = \frac{1}{3}h \left( S_{\triangle DEF} + S_{\triangle HIJ} + (S_{\triangle DEF} S_{\triangle HIJ})^{1/2} \right) \quad (13)$$

with  $h$  denoting the height of the half-layer chamber. Moreover,  $S_{\triangle DEF}$  is the top-face area of the pentahedron, which varies with the height changes. As well,  $S_{\triangle HIJ}$  represents the bottom face area of the pentahedron, which is constant, regardless of the height changes.

Moreover,  $V_t$  represents the volume of each added triangular pyramid outside the origami structure. Since  $\triangle ABD$  is assumed to be constant during the morphing process, the three pyramids bear the same volume, namely

$$V_t = \frac{1}{3}h S_{\triangle ABH} \quad (14)$$

where  $S_{\triangle ABH}$  denotes the constant base area of the added triangular pyramid.

As shown in Fig. 5(d),  $D'$  represents the projection of vertex  $D$  on the bottom plane. The length of the virtual crease  $D'G$  can

be expressed as

$$l_{D'G} = (l_{DG}^2 - h^2)^{1/2} \quad (15)$$

where  $l_{DG}$  denotes the length of the virtual crease  $DG$ , which is a constant and can be derived from the known parameters.

The stretchable crease  $DE$  remains parallel to the bottom plane during the morphing process. Hence, its projection on the bottom plane  $D'E'$  bears the same length as  $DE$ . Therefore, the length of the stretchable crease  $DE$  can be expressed as

$$l_{DE} = \sqrt{3}(l_{D'G} + l_{GO}) = \sqrt{3} \left( \frac{1}{4}a^2 \tan^2 \theta - h^2 \right)^{1/2} + \frac{3}{2}a. \quad (16)$$

Substituting (13), (14), and (16) into (12), the internal volume of the origami chamber is obtained as

$$V = -\frac{\sqrt{3}}{4}h^3 + f(h) + a_1h \quad (17)$$

where  $f(h)$  is a function of the height  $h$ , defined as

$$f(h) = \frac{3}{4}ah \left( (-h^2 + a_2)^{1/2} + (-h^2 + \sqrt{3}a(-h^2 + a_2)^{1/2} + a_3)^{1/2} \right) \quad (18)$$

with constants  $a_1$ ,  $a_2$ , and  $a_3$ , defined as follows:

$$\begin{aligned} a_1 &= \left( \frac{11\sqrt{3}}{16} + \frac{\sqrt{3}}{16} \tan^2 \theta \right) a^2 \\ a_2 &= \left( \frac{1}{4} \tan^2 \theta \right) a^2 \\ a_3 &= \left( \frac{3}{4} + \frac{1}{4} \tan^2 \theta \right) a^2. \end{aligned} \quad (19)$$

Then, substituting (17) into (11), the output force of the origami chamber is obtained as

$$F = \frac{3\sqrt{3}}{4}Ph^2 - Pg_1(h) - Pg_2(h) - Pg_3(h) - Pa_1 \quad (20)$$

with the definitions as follows:

$$\begin{aligned} g_1(h) &= \frac{-6ah^2 + 3aa_2}{4(-h^2 + a_2)^{1/2}} \\ g_2(h) &= \frac{-6ah^2 + 3aa_3}{4(-h^2 + \sqrt{3}a(-h^2 + a_2)^{1/2} + a_3)^{1/2}} \\ g_3(h) &= \frac{-9\sqrt{3}a^2h^2 + 6\sqrt{3}a^2a_2}{8(-h^2 + a_2)^{1/2} (-h^2 + \sqrt{3}a(-h^2 + a_2)^{1/2} + a_3)^{1/2}}. \end{aligned} \quad (21)$$

Equation (20) reveals the correlations of the input pressure, the deployment height, and the output force of the origami chamber.

The variation interval of the output force can then be predicted at a given pressure and a specific range of deployment. Moreover, the output force can be adjusted along with the deployment via the active regulation of the input pressure through the proportional valve. The aforementioned model illustrates the capability

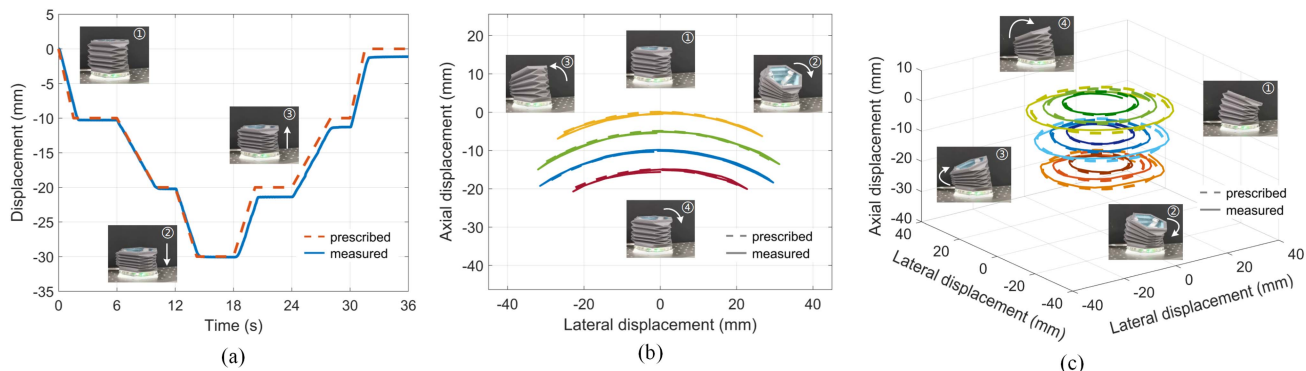


Fig. 6. Tracking performance. Dash lines represent the prescribed trajectories; solid lines represent the measured ones. (a) Line trajectory with variable speed. (b) Four arc trajectories with the initial heights [ $h$  in Fig. 4(b)] of 35, 40, 45, and 50 mm. (c) Nine circular trajectories with the initial heights of 30, 40, 50 mm and the diameters of 20, 30, 40 mm.

to both control the output force to realize weight-lifting maneuvers and to adjust the actuator stiffness by suitably tuning the antagonistic force.

## V. EXPERIMENTAL VALIDATION

### A. Experimental Setup

The objective of the proposed design is to achieve controllable three-dof motion with relatively high positioning accuracy and variable stiffness. Thus, in order to validate the proposed design principle and demonstrate the unique capabilities of the actuator, several tests on the tracking performance, stiffness characterization, static force characterization, and weight-lifting performance, were conducted. Moreover, the multimodule behavior was also tested to demonstrate the modularity and the potential applications of the actuator.

The experiments were conducted with a module prototype. The pneumatic source inflated the prototype through a soft silicon tube. The input pressure was regulated by an off-board proportional valve (ITV1010, SMC), in combination with a pressure sensor (PSE532, SMC). The on-board micromotors and the proportional valve were synchronously controlled with pulswidth modulation signals, generated by an off-board microcontroller (Mega 2560, Arduino). A digital to analog converter (DAC) module (DC2376 A, ADI) was connected between the controller and the proportional valve, to provide a stable voltage input. Such a closed-loop system could keep the inner pressure of the chamber around the prescribed value during the motion. The micromotors, with assembled Hall encoders, realized the position and velocity control of the tendon-driven system, based on a cascaded feedback proportional-integral (PI) controller. As to the measurement instruments, the three-dof motion of the proposed actuator was measured by a motion capture system (OptiTrack Prime 41), with an absolute measurement accuracy around 0.3 mm. A force sensor (Mini 45, ATI), fixed upon the end effector of a six-dof industrial robot (UR 10), was used to measure the interaction force, to demonstrate the stiffness characterization of the actuator. For the blocking-force measurements, a universal testing machine (5966, Instron) was utilized.

### B. Tracking Performance

To demonstrate the controllable versatile motion and validate the proposed kinematic model, three different kinds of trajectories were prescribed to test the tracking performance of the actuator, under a low input pressure value of around 3 kPa. First, a line trajectory with variable speed was tested. The three micromotors were controlled simultaneously with the same input so that the actuator should exhibit contraction and extension. As shown in Fig. 6(a), the result exhibited small positioning errors of 0.19 mm in the contraction, and 1.27 mm in the extension, with well-controlled motion speeds from 2.5 to 6.5 mm/s. The 1.08-mm error offset in the extension process may be mainly caused by the manually assembled Hall encoders, as well as the backlash of the micromotors and the worm gears. In addition, it should be noted that the motion speed was restricted by the maximum speed of the motors, which could be further improved by changing the three motors with others showing a better performance.

As described in the previous sections, the actuator can produce a 1T2R motion including extension, contraction, and omnidirectional bending. The latter can be regarded as a rotation around any radial direction, i.e., the moving platform can rotate about any specific axis parallel to the  $Oxy$ -plane, and execute a circular swing around the  $z$ -axis, as depicted in Fig. 4(b). Hence, two kinds of trajectories, the arcs perpendicular to the  $Oxy$ -plane and the circles parallel to the  $Oxy$ -plane, were selected to both test the bending performance and validate the kinematic model.

As shown in Fig. 6(b), the moving platform of the actuator was first set to move along four arc trajectories whose axes of rotation lie at four different heights. The actuator was set to execute a reciprocating motion, starting from the straight configuration in each test. The measured trajectories showed good agreement with the prescribed ones. The mean positioning errors were 0.80, 1.27, 1.18, and 1.06 mm for four different heights. As a consequence, there was no obvious indication that the height of the moving platform affected the tracking performance. Additionally, nine circular trajectories, at three different heights and with three different diameters, were tested. As shown in Fig. 6(c), the experimental process, as well as the

results, demonstrated high motion versatility and controllability of the actuator. The positioning errors grew with the height and the diameter. The error accumulation during the circular motions might have caused this effect. However, considering the motion range in each limb of the parallel endoskeleton, as well as our manual fabrication method, the actuator proved to exhibit an acceptable positioning accuracy, based on the proposed kinematic model.

### C. Stiffness Characterization

To demonstrate the variable stiffness and validate the effectiveness of the proposed antagonistic actuation system, stiffness tests under four different conditions were conducted. As shown in Fig. 7, both the axial and the lateral stiffness of the prototype were tested, with an initial actuator length of 60 and 90 mm. In each case, the origami chamber was actuated with a supply pressure of 0, 3, 5, and 8 kPa, to generate different but not excessive antagonistic forces, according to our quasi-static model. The prototype was placed on a fixed platform during the tests; reciprocating passive deformations were imposed by the industrial robot, with a force sensor fixed on its end effector. In this way, the force–displacement relations of the prototype could be recorded under all conditions. The stiffness variation under different pressure values were measured; the influence of the initial length was also evaluated.

The plots in Fig. 7(a) illustrate the forces generated with four different pressure values in the first condition, namely, axial pressing with an initial actuator length of 60 mm. The unpressurized prototype exhibited noticeable axial compliance, which generated 4.2 N with an axial displacement of 4 mm. On the contrary, the stiffness of the prototype increased significantly when pressurized. The 4-mm axial displacement generated around 24 N when the prototype was actuated with a supply pressure of 3 kPa, about 5 times the unpressurized condition. Further, the interaction force rose to 54 N when the pressure increased to 8 kPa, close to 13 folds of the unpressurized condition. It should be noted that the 3-kPa pressure is the lowest supply pressure of our proportional valve; 8 kPa is still an extremely low pressure. In consideration of the commonly used input pressure of other SPAs (from tens to hundreds of kilopascal), the low demand for air pressure makes the proposed actuator much safer, more energy efficient, and with more potential to be untethered [73], [74], [75].

The axial stiffness, with an initial actuator length of 90 mm, was then measured as a contrast. The results shown in Fig. 7(b) indicate that the generated forces had no obvious difference from the previous ones. The generated force of the unpressurized prototype reduced to 2.4 N, with an axial displacement of 4 mm, due to the deformation decrease of the silicon rubber panels integrated inside the parallel endoskeleton. As a consequence, the force of the 8-kPa pressurized prototype (57.7 N) reached 24 times the value of the unpressurized condition. In addition, the increment of the initial actuator length also reduced the hysteresis of the prototype. The larger volume of the origami chamber might contribute to such a phenomenon, because the

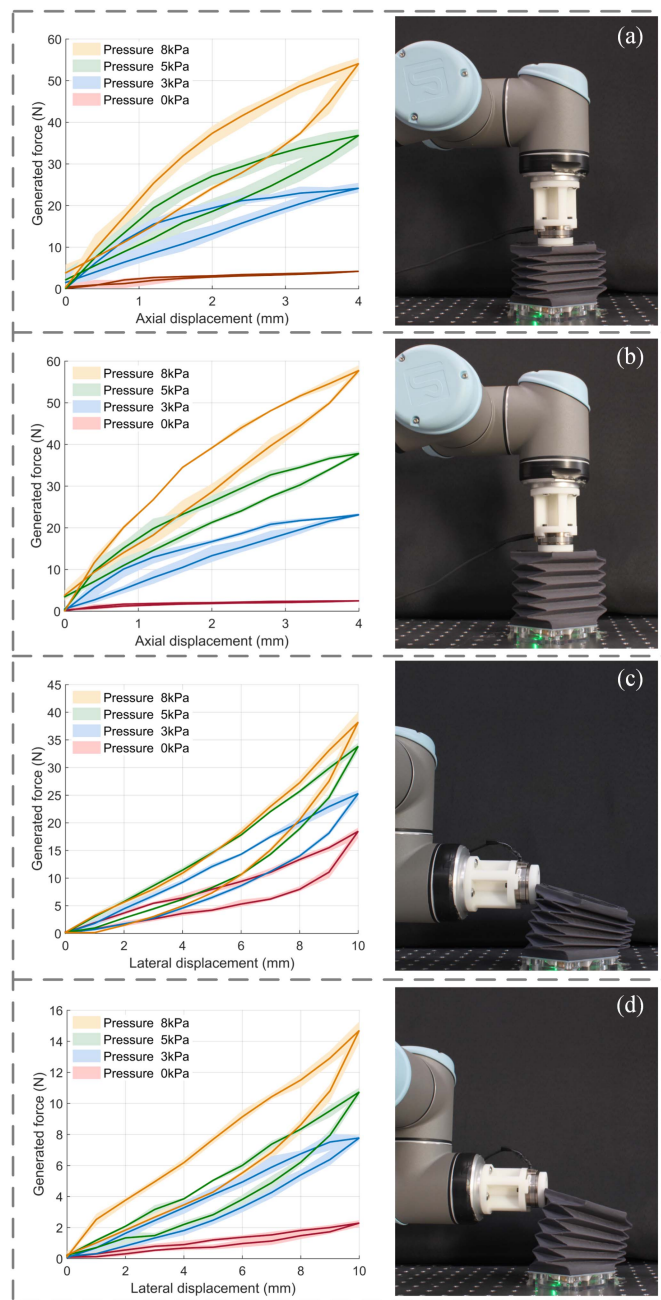


Fig. 7. Force-deformation curves obtained during the stiffness characterization test and the experimental setup. (a) Axial press with the initial actuator length of 60 mm. (b) Axial press with the initial actuator length of 90 mm. (c) Lateral push with the initial actuator length of 60 mm. (d) Lateral push with the initial actuator length of 90 mm.

4-mm deformation process of the larger chamber caused a relatively lower variation of the internal volume.

Further, the industrial robot was driven to laterally knock the prototype; the lateral stiffness was measured accordingly. The plots in Fig. 7(c) and (d) illustrate the results with initial actuator lengths of 60 and 90 mm, respectively. Apparently, the stiffness variation was still evident, along with the change of the supply pressure. The actuator with smaller initial length exhibited a higher lateral stiffness. This was mainly caused by

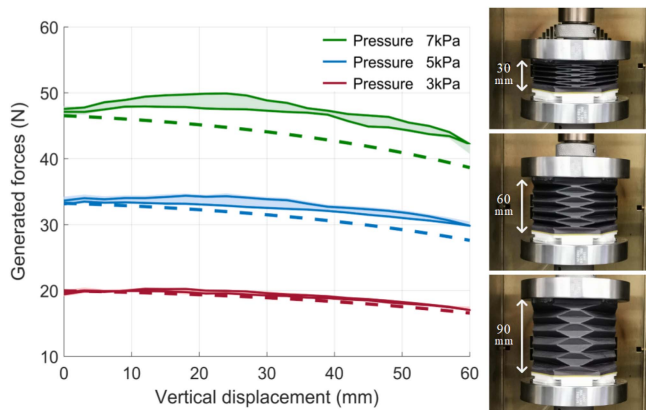


Fig. 8. Force-deformation curves obtained during the static force characterization test. Dash lines represent the predicted results; solid lines with error shadow represent the measured ones. The 30-mm actuator length is defined as the initial position, namely the vertical displacement at this point is 0.

the smaller moment arm of the external force, as well as the larger deformation of the silicon rubber panels. When the initial length increased to 90 mm, the generated force of the unpressurized prototype decreased to 2 N, with a lateral displacement of 10 mm, thus showing a superior structural compliance. At the same time, the stiffness can also be enhanced more than 7 times with a supply pressure of 8 kPa, which ensured the manipulation capability of the proposed actuator. It should be noted that the maximum working pressure of the current unloaded prototype is limited to 12 kPa by the fracture of the small 3-D-printed connectors of the endoskeleton, since an increase of the input pressure would convert into that of the internal force.

#### D. Static Force Characterization

To demonstrate the force output capacity and validate the proposed quasi-static model, a universal testing machine was used to constrain the origami chamber at different lengths, and measure the output forces under different input pressure values. During the measurement process, the base platform of the origami chamber was vertically fastened to the stationary clamp of the universal testing machine. The movable clamp of the machine pressed the output platform of the origami chamber to the whole actuator length of 30 mm, namely the fully contracted configuration, and set it as the initial position. Then, the heights of the deployed origami chamber were determined by the actively controlled vertical displacement of the movable clamp; the output forces, generated by the input pressure, were recorded at different heights.

Fig. 8 illustrates the experimental process, as well as the comparison between the measured results and the predicted ones based on the quasi-static model, under three different input pressure values. The measured relations between the vertical displacement and the output force showed an acceptable agreement with the predicted values, which means the proposed model is effective and can be used for the control of the proportional valve. It can be also noticed that the accuracy of the proposed model is relatively higher with a lower input pressure. Such phenomenon

may be mainly caused by the inconspicuous deformation of the rigid carbon fiber sheets of the origami chamber, which is ignored in the proposed model. Such deformation will expand the internal volume of the origami chamber, thereby increasing the output force. Additionally, it is noteworthy that the output force exhibited small variations, along with the passive vertical displacement under specific input pressure. The variations can be compensated based on the proposed model, which means the actuator can be potentially used to realize constant force output with a controllable working length. Therefore, this actuator has the potential to replace the expensive, commercial active contact flange that is widely used in the field of surface treatment.

#### E. Weight-Lifting Performance

As stated previously, the input pressure can adjust the stiffness and the output thrust force of the actuator. Since the actuator is able to generate translational motion and thrust force, it should be capable of producing bottom-up weight-lifting maneuvers. Hence, the weight-lifting performance was tested to validate such capability, and to demonstrate that the motion can still be precisely controlled upon loading.

The actuator was placed vertically with different weights loaded on its moving platform during the experiments, then set to track prescribed trajectories. The experimental results, as well as the real-time conditions, are shown in Fig. 9. It is apparent from Fig. 9(a)–(c) that the position and the velocity of the actuator were fully under control with weights from 1 to 3 kg. The 1-mm error in the lowest part of Fig. 9(a) was mainly caused by the higher internal force, due to the 3-kPa limitation of the proportional valve, which was expected to be lower under 1-kg weight. Such error diminished when the load increased to 2 or 3 kg. However, the stability of the translational motion decreased slightly, since larger weights led to higher moments on the output platform of the actuator. As a consequence, the bottom-up weight-lifting capability was constrained to 3 kg by the accompanied moment from the weights; this capability can be improved with more stable weights to be used in the test. However, it is noteworthy that the 3-kg weight-lifting capability is still acceptable. Considering the weight of the whole actuator (301.4 g) and that of the origami chamber (57.5 g), the actuator proved to be capable of pushing up tenfold its self-weight and 52-fold the weight of the origami chamber. It is worth noting that such a weight-lifting performance benefits from both the hybrid structure and the hybrid actuation method. The parallel mechanism and the inserted tendons contribute more to motion control; the origami chamber and the pneumatic pressure support a higher payload and form a compliant, modular structure. Neither the tendon-driven mechanism (see Fig. A2 in the Supplementary Material) nor the pneumatic origami chamber (see Fig. A3 in the Supplementary Material) alone can execute such controllable motions under payload.

The input pressure values were calculated based on the quasi-static model to balance different payloads during whole motion ranges, and regulated by the proportional valve and the pressure sensor. It is worth noting that the setting load of the model is the sum of the actual payload and a small preload, to obtain a higher

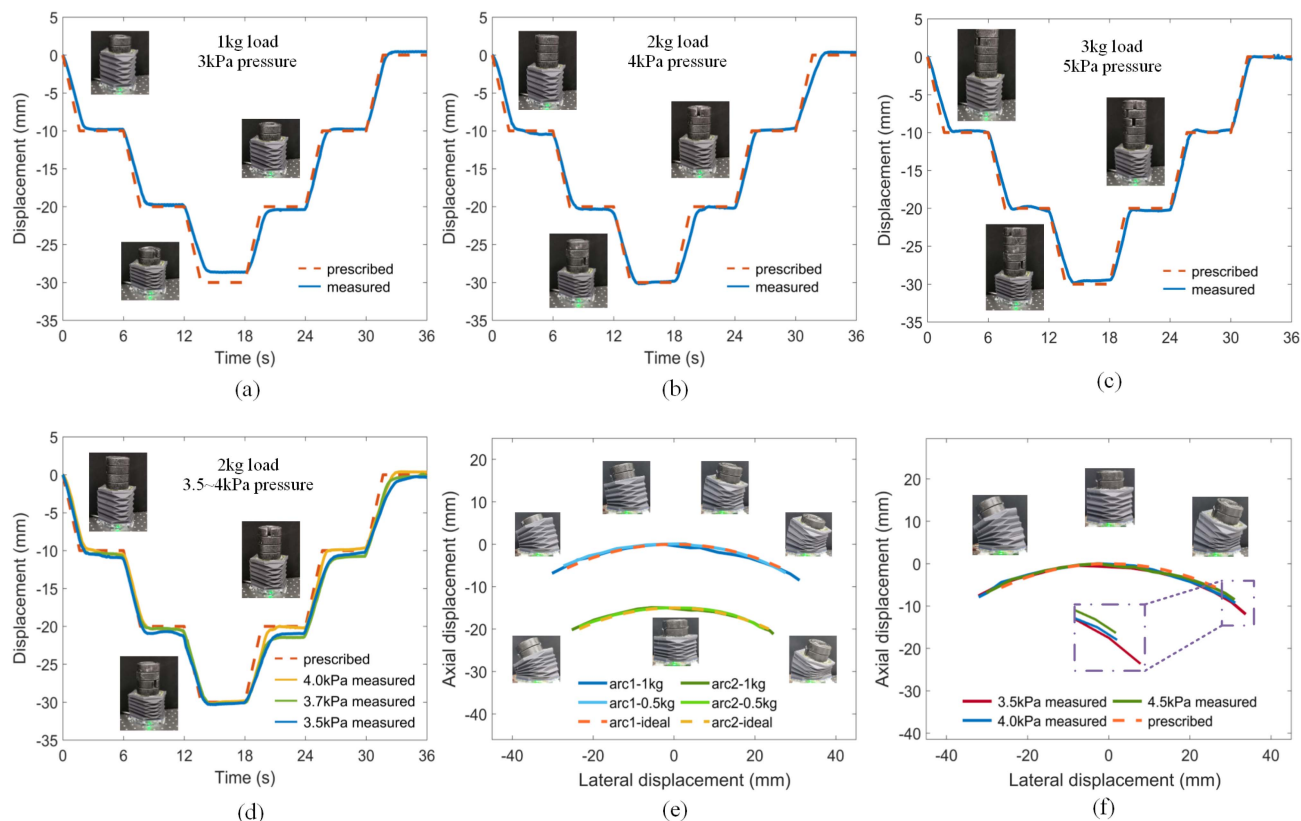


Fig. 9. Weight-lifting performance. (a)–(c) Tracking performances loaded with different weights of 1, 2, and 3 kg. (d) Tracking performances with different input pressures of 3.5, 3.7, and 4.0 kPa, when loaded with 2-kg weights. (e) Bending performances loaded with different weights of 0.5 and 1 kg. (f) Bending performances with different input pressures of 3.5, 4.0, and 4.5 kPa, when loaded with 1-kg weights.

stiffness. To validate the effect of the actuator stiffness, the influence of the input pressure on the weight-lifting maneuver was further tested. The plots in Fig. 9(d) show the trajectories of the actuator loaded with 2-kg weights, with input pressures of 3.5, 3.7, and 4.0 kPa. It was apparent that higher input pressure values exhibited better stability during the contraction process, since the pneumatic force carries more external loads. Moreover, the response speed, as well as the accuracy, was also improved by the higher pressure value during the extension process. As a result, the balance between the soft and the rigid actuation can be modulated according to the working condition, while the motion performance can benefit from a higher stiffness. However, the input pressure should not be set too high, especially under small payloads, since it risks bringing about an unbearable load on the tendon-driven system (see Fig. A4 in the Supplementary Material).

In addition to translational motion, the weight-lifting bending performance was also tested. It has been demonstrated in Fig. 7 that the increment of the pressure value contributed more to the axial stiffness than to the lateral one. Hence, lighter weights were utilized during the bending tests. As shown in Fig. 9(e), the moving platform of the actuator was set to move along two arc trajectories at different heights, loaded with 0.5 and 1-kg weights, respectively. Overall, the measured trajectories still showed good agreement with the prescribed ones. The moving platform went further at the bending boundaries when loaded

with 1 kg than that loaded with 0.5 kg. This phenomenon should be mainly caused by the moment generated from the external weights. It was also more evident at the higher arc trajectories, due to the existence of a larger moment arm.

Later, to further validate the effect of the actuator stiffness on the weight-lifting bending, the influence of the input pressure was tested. The higher arc trajectory was utilized to make the difference more distinct. The plots in Fig. 9(f) demonstrate the measured trajectories of the actuator loaded with 1-kg weights and input pressures of 3.5, 4.0, and 4.5 kPa. In general, all the three trajectories demonstrated acceptable tracking performance. However, it was apparent that the moving platform went further at the bending boundaries, along with the reduction of the pressure value. The actuator could attain a higher stiffness with a higher pressure, then showing better resistance to the external moment.

It can be noticed from the weight-lifting bending tests that a higher external moment will reduce the accuracy of the actuator, while a higher input pressure will improve it. Such a phenomenon is a specific feature of the proposed hybrid-driven system. When partial compression occurs due to the passive compliance and the external moment, the tendon inside the compressed linkage will loosen, since the tendon can only generate tensile force. Although the positioning accuracy can be reduced, such kind of passive compliance generated by this hybrid-driven system provides more interaction friendliness.

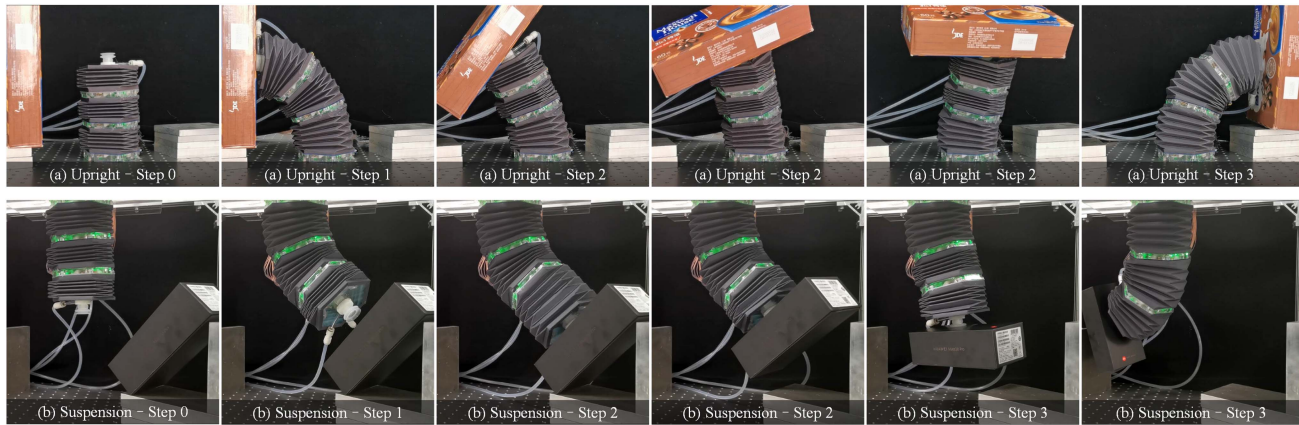


Fig. 10. Multimodule pick-and-place manipulation. Two different modes of manipulation were tested and different trajectories were utilized. (a) Upright manipulation. Step 1: The three modules executed extension and bending; step 2: The first module executed circular swing and other two modules executed contraction; and step 3: The first module kept stable and other two modules executed extension and bending. (b) Suspension manipulation. Step 1: The first two modules executed extension and bending, and the third module kept stable; step 2: The first two modules kept stable, and the third module executed extension and contraction; step 3: The first two modules executed bending, and the third module executed extension and bending.

Moreover, the passive deformation can also be compensated by actively increasing the input pressure. It should be noted that the control scheme of the current prototype is open-loop at the whole actuator level. The passive deformation can be detected and actively compensated if closed-loop feedback control is realized by adding sensing elements inside the actuator.

#### F. Multimodule Behavior Test

Considering the motion capability and the modular structure of the proposed actuator, three actuators were connected in series via hot melt adhesive that is readily peeled off, then forming a modular continuum manipulator to demonstrate the potential applications of the actuator. The motion and the stiffness of each actuator were individually controlled during the test. The third module was equipped with a suction cup for controllable attachment and detachment to objects. It should be noted that the numbers of proportional valve, pressure sensor, and micro-controller were all increased by a factor of three.

1) *Pick-and-Place Manipulation*: The proposed actuator can generate both tensile and thrust force, due to the antagonistic actuation from the tendons and the positive pressure. Thus, two different kinds of pick-and-place manipulation tests, namely, upright manipulation and suspension manipulation, were demonstrated as described in the following.

The first test involved vertically placing the three-module continuum manipulator on a fixed platform, and relocating the object from the starting location to the target one. As shown in Fig. 10(a), the initial configuration of the manipulator was fully contracted. Then, the manipulator reached the object via the shape-morphing (extension and bending) of all three modules. After picking up the object by actively depressurizing the suction cup, the second and the third module contracted back to the initial configuration, while the first module was kept bent. Later, the first module was set to move along a circular trajectory, until the bending of the manipulator was directed toward the target location. Finally, the second and the third modules extended

and bent toward another direction, in order to place the object steadily on the target location. Different motion types like contraction, extension, omnidirectional bending, and circular swing, were all displayed during this manipulation process. The versatility of the proposed actuator was proved to enrich the motion capability of the multimodule manipulator. Moreover, the balance between compliance and stiffness also contributed to the upright manipulation tasks, which means the stiffness of the manipulator was capable of finishing the transfer task vertically, while the compliance of the manipulator ensured the shape-morphing process.

The second test consisted in finishing a pick-and-place manipulation task with another trajectory. The three-module continuum manipulator was hanging on a fixed platform, opposite to the former placement. As shown in Fig. 10(b), the initial configuration of the manipulator was still fully contracted, while the suction cup faced toward the ground. The third module was kept contracted, as the first two modules extended and bent until the suction cup was set parallel to the object. Then, the third module extended to reach the object and picked it up via contraction. Finally, all the modules bent toward the opposite direction to transfer the object to the target location. Unlike the former test, the tensile force from the tendons contributes more to the load-carrying capacity in the suspension manipulation. However, the stiffness generated by the antagonistic actuation was still indispensable to hold the morphing shape during the weight-lifting bending and the oblique extension of the modules. As a consequence, both the controllable versatile motion and the stiffness characterization improved the functionality of the actuator. The serially connected modular continuum manipulator also benefited from these features, and could accordingly finish controlled pick-and-place tasks in various modes.

It is noteworthy that motion versatility and workspace can be enhanced upon increasing the number of individually controlled modules. However, further extension also yields problems of dead-weight, which will make the first modules bear a higher

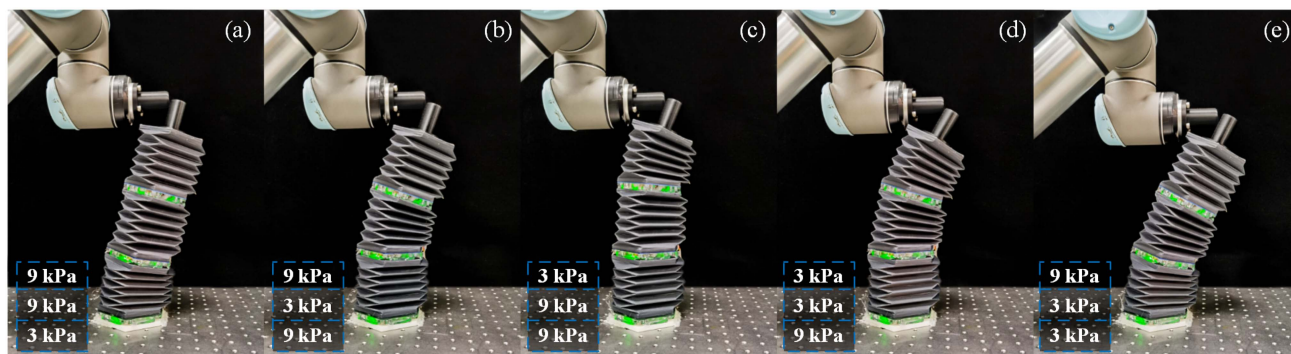


Fig. 11. Multimodule partially adjustable stiffness. Five different combinations of high and low input pressure were tested. (a) First module 3 kPa, second module 9 kPa, and third module 9 kPa. (b) First module 9 kPa, second module 3 kPa, and third module 9 kPa. (c) First module 9 kPa, second module 9 kPa, and third module 3 kPa. (d) First module 9 kPa, second module 3 kPa, and third module 3 kPa. (e) First module 3 kPa, second module 3 kPa, and third module 9 kPa.

load, thereby affecting their performance. Hence, further enhancement of the modularity and scalability also requires lighter, stiffer materials for the endoskeleton, besides micromotors with better performance. The load-carrying capability (especially in the suspension manipulation) of the proposed actuator will be further enhanced if the motors can output higher torque. Moreover, if the working condition requires high load-carrying capacity and has no restriction on the manipulator volume, the actuators can be readily scaled-up, as few standard parts would be needed. Then, larger motors with better performance can be employed.

2) *Partially Adjustable Stiffness*: The motion versatility, generated by the independently controlled three-dof motion of the three modules, was demonstrated in the pick-and-place tasks. Similarly, the independently controlled stiffness could also improve the performance of the multimodule continuum manipulator [58], [76].

Fig. 11 illustrates the behavior test on the selective mechanical tuning capability of the three-module manipulator. The manipulator was vertically placed onto a fixed platform, just as in the upright manipulation test. Then, an external force generated by an industrial robot was applied to the output bar connected with the moving plate of the third module, to produce passive deformation of the whole manipulator. During the test, different input pressures were applied to different modules, to verify the possibility of partially tuning the stiffness level. As shown in Fig. 11(a), the first module was supplied with a 3-kPa input pressure, while the other two modules were supplied with 9 kPa. It was apparent that the first module with relatively lower input pressure performed most of the deformation; the other two modules, with higher pressure, almost kept straight during the passive deformation. Then, the second and the third modules became those with the lower pressure, respectively. Their deformation state changed accordingly; the passive motion range of the manipulator also changed significantly, which can be noticed from Fig. 11(b) and (c). As a consequence, the stiffness of the continuum manipulator was proved to be partially adjustable. Further combinations of the independently controlled stiffness could further generate more forms of passive deformation, as depicted in Fig. 11(d) and (e). Since safe

interaction and load-bearing bring about completely different requirements for continuum manipulators, such a capability can make the manipulator capable of executing various operations in the presence of interference from external loads. Although the current tests only exerted actions on the distal end, the compliant origami chamber can also prevent the inner mechanism from being disturbed by external obstacles under a low force and generate passive deformation under a high force, similar to the present situation. The interaction between a human hand and the proposed continuum manipulator with partially adjustable stiffness is also demonstrated in the Supplementary Video. The deformation state will be more varied if the manipulator consists of a higher number of modules.

## VI. CONCLUSION

In this article, a rigid-soft hybrid origami actuator, inspired by the physiological structure of vertebrates, was introduced. The pneumatic origami chamber, together with the tendon-driven endoskeleton, formed an inner rigid/outer soft hybrid structure and an antagonistic actuation system that can produce a specific motion with the required stiffness. A prototype was built based on novel, replicable fabrication methods of both the origami chamber and the parallel endoskeleton. The motion, as well as the stiffness of the prototype, can be effectively controlled based on both kinematic and quasi-static analyses. Experiments on motion capability, stiffness variation, static force output, weight-lifting maneuver, and multimodule behavior were conducted.

The results showed that a single proposed actuator can exhibit various motion types, including extension, contraction, omnidirectional bending, and circular swing. All these motions were fully controllable based on the symbolic kinematic model of the rigid parallel endoskeleton, unlike other current designs of SPAs. The mean positioning errors of the unidirectional and bidirectional translational motions were 0.19 and 0.73 mm, while the positioning accuracy of the bending motion was still comparable. As to the variable stiffness, up to 24 times axial variation and 7 times lateral variation can be realized with a small input pressure range of 0–8 kPa. The hybrid actuation, as well as the hybrid structure, prompted the actuator to produce

accurate translational motion when loaded with a 3-kg weight, which was ten times the weight of the whole actuator and 52 times the weight of the origami chamber. Other merits included high extension ratio, low threshold pressure, no radial expansion, and better air leakage resistance (see the Supplementary Video), which benefit from the rigid-soft hybrid origami chamber, consisting of discrete carbon fiber sheets and unstretchable fabric. Owing to the distinctive features and the modular structure of the proposed actuator, a continuum manipulator can be obtained by connecting three actuators in series. Accordingly, the manipulator can perform controllable pick-and-place manipulations in various manners and adjust the stiffness of each module independently.

This work proposed a design concept of integrating tendon-constrained parallel mechanisms into soft pneumatic chambers and forming an antagonistic actuation system, which built a bridge between conventional rigid parallel mechanisms and novel soft actuators. The proposed design, fabrication, and modeling methods will provide guidelines to explore more kinds of hybrid actuators with various motion types and unique features, considering the various topologies of the existing designs of parallel mechanisms. Considering the present actuator's capability of achieving precise, multimode motion as an intrinsically compliant actuator, meanwhile capable of load-carrying, compliance-needed, or human-involved object manipulations should be the most suitable application. Its modular and scalable feature renders both a larger workspace (serially connecting more actuators) and miniaturization (using pop-up methods to fabricate the mechanism) achievable, while powerful micromotors are also desired. Using smart materials like SMA or twisted and coiled polymer (TCP) to replace the motor-driven cables will highly contribute to the miniaturization of the present actuator, while the precise control of their length is still challenging. Multimodal locomotion should be another suitable application, since its multi-dof motion renders multigait crawling and direction turning readily achievable. Meanwhile, the fabric-based origami chamber requires low pressure to inflate, thus the untethered upgrading should be a primary focus of future work, to get rid of the tubes directly connected to the modules. Moreover, the closed-loop control of the current design is realized on the motor level, i.e., Hall encoders were assembled on the motor to realize the position and velocity control of the tendon-driven system based on a cascaded feedback PI controller. In future work, sensing elements like liquid metal or AgNWs can be integrated inside the silicon rubber panel of the foldable linkage, to realize closed-loop feedback control at the whole actuator level and further improve the motion accuracy. In addition, lighter materials with higher stiffness can also be applied to construct the endoskeleton, to withstand higher antagonistic forces for a larger range of variable stiffness.

#### ACKNOWLEDGMENT

The authors would like to thank Prof. J. Paik (EPFL), Prof. J. Hughes (EPFL), Prof. H. Zhao (THU), Prof. M. Tolley (UCSD), Dr. J. Zou (SJTU), and Dr. L. Mao (SJTU), for their permissions to use images of their works. The authors would also like to thank

Dr. I. Lu (IC/FDU) for the suggestions related to presentation and Dr. K. Chen (SJTU) for the discussion related to modeling.

#### REFERENCES

- [1] D. Rus and M. T. Tolley, "Design, fabrication and control of soft robots," *Nature*, vol. 521, no. 7553, 2015, Art. no. 467.
- [2] C. Laschi, B. Mazzolai, and M. Cianchetti, "Soft robotics: Technologies and systems pushing the boundaries of robot abilities," *Sci. Robot.*, vol. 1, no. 1, 2016, Art. no. aah3690.
- [3] P. Polygerinos et al., "Soft robotics: Review of fluid-driven intrinsically soft devices; manufacturing, sensing, control, and applications in human-robot interaction," *Adv. Eng. Mater.*, vol. 19, no. 12, 2017, Art. no. 1700016.
- [4] Z. Zhang, Y. Long, G. Chen, Q. Wu, H. Wang, and H. Jiang, "Soft and lightweight fabric enables powerful and high-range pneumatic actuation," *Sci. Adv.*, vol. 9, no. 15, 2023, Art. no. eadg1203.
- [5] W. Wang, R. N. Loh, and E. Y. Gu, "Passive compliance versus active compliance in robot-based automated assembly systems," *Ind. Robot, Int. J.*, vol. 25, no. 1, pp. 48–57, 1998.
- [6] R. Van Ham, T. G. Sugar, B. Vanderborght, K. W. Hollander, and D. Lefeber, "Compliant actuator designs," *IEEE Robot. Automat. Mag.*, vol. 16, no. 3, pp. 81–94, Sep. 2009.
- [7] F. Ilievski, A. D. Mazzeo, R. F. Shepherd, X. Chen, and G. M. Whitesides, "Soft robotics for chemists," *Angewandte Chemie Int. Ed.*, vol. 50, no. 8, pp. 1890–1895, 2011.
- [8] R. F. Shepherd et al., "Multigait soft robot," *Proc. Nat. Acad. Sci.*, vol. 108, no. 51, pp. 20400–20403, 2011.
- [9] M. T. Tolley et al., "A resilient, untethered soft robot," *Soft Robot.*, vol. 1, no. 3, pp. 213–223, 2014.
- [10] P. Polygerinos et al., "Modeling of soft fiber-reinforced bending actuators," *IEEE Trans. Robot.*, vol. 31, no. 3, pp. 778–789, Jun. 2015.
- [11] T. Ranzani, M. Cianchetti, G. Gerboni, I. D. Falco, and A. Menciassi, "A soft modular manipulator for minimally invasive surgery: Design and characterization of a single module," *IEEE Trans. Robot.*, vol. 32, no. 1, pp. 187–200, Feb. 2016.
- [12] A. D. Marchese and D. Rus, "Design, kinematics, and control of a soft spatial fluidic elastomer manipulator," *Int. J. Robot. Res.*, vol. 35, no. 7, pp. 840–869, 2016.
- [13] J. Fras, Y. Noh, M. Macias, H. Wurdemann, and K. Althoefer, "Bio-inspired octopus robot based on novel soft fluidic actuator," in *Proc. IEEE Int. Conf. Robot. Automat.*, 2018, pp. 1583–1588.
- [14] Z. Xie et al., "Octopus arm-inspired tapered soft actuators with suckers for improved grasping," *Soft Robot.*, vol. 7, no. 5, pp. 639–648, 2020.
- [15] D. S. Shah, J. P. Powers, L. G. Tilton, S. Kriegman, J. Bongard, and R. Kramer-Bottiglio, "A soft robot that adapts to environments through shape change," *Nature Mach. Intell.*, vol. 3, no. 1, pp. 51–59, 2021.
- [16] E. Perez-Guagnelli, J. Jones, and D. D. Damian, "Hyperelastic membrane actuators: Analysis of toroidal and helical multifunctional configurations," *Cyborg Bionic Syst.*, vol. 2022, 2022, Art. no. 9786864.
- [17] J. Zou et al., "Muscle-fiber array inspired, multiple-mode, pneumatic artificial muscles through planar design and one-step rolling fabrication," *Nat. Sci. Rev.*, vol. 8, no. 10, 2021, Art. no. nwab048.
- [18] T. George Thuruthel, Y. Ansari, E. Falotico, and C. Laschi, "Control strategies for soft robotic manipulators: A survey," *Soft Robot.*, vol. 5, no. 2, pp. 149–163, 2018.
- [19] A. A. Stokes, R. F. Shepherd, S. A. Morin, F. Ilievski, and G. M. Whitesides, "A hybrid combining hard and soft robots," *Soft Robot.*, vol. 1, no. 1, pp. 70–74, 2014.
- [20] S. W. Kwok et al., "Magnetic assembly of soft robots with hard components," *Adv. Funct. Mater.*, vol. 24, no. 15, pp. 2180–2187, 2014.
- [21] Y. Tang et al., "Leveraging elastic instabilities for amplified performance: Spine-inspired high-speed and high-force soft robots," *Sci. Adv.*, vol. 6, no. 19, 2020, Art. no. aaz6912.
- [22] Y. Chen, F. Wan, T. Wu, and C. Song, "Soft-rigid interaction mechanism towards a lobster-inspired hybrid actuator," *J. Micromechan. Microeng.*, vol. 28, no. 1, Dec. 2017, Art. no. 014007.
- [23] J. Zhang et al., "Geometric confined pneumatic soft-rigid hybrid actuators," *Soft Robot.*, vol. 7, no. 5, pp. 574–582, 2020.
- [24] D. Rus and M. T. Tolley, "Design, fabrication and control of origami robots," *Nature Rev. Mater.*, vol. 3, no. 6, pp. 101–112, 2018.
- [25] D. Rus and C. Sung, "Spotlight on origami robots," *Sci. Robot.*, vol. 3, no. 15, 2018, Art. no. aat0938.

- [26] M. Salerno, K. Zhang, A. Menciassi, and J. S. Dai, "A novel 4-DoF origami grasper with an SMA-actuation system for minimally invasive surgery," *IEEE Trans. Robot.*, vol. 32, no. 3, pp. 484–498, Jun. 2016.
- [27] Z. Zhakypov and J. Paik, "Design methodology for constructing multimaterial origami robots and machines," *IEEE Trans. Robot.*, vol. 34, no. 1, pp. 151–165, Feb. 2018.
- [28] S. R. Kim, D. Y. Lee, S. J. Ahn, J. S. Koh, and K. J. Cho, "Morphing origami block for lightweight reconfigurable system," *IEEE Trans. Robot.*, vol. 37, no. 2, pp. 494–505, Apr. 2021.
- [29] W. Kim et al., "Bioinspired dual-morphing stretchable origami," *Sci. Robot.*, vol. 4, no. 36, 2019, Art. no. aay3493.
- [30] J. Santoso, E. H. Skorina, M. Luo, R. B. Yan, and C. D. Onal, "Design and analysis of an origami continuum manipulation module with torsional strength," in *Proc. IEEE/RSJ Int. Conf. Intell. Robots Syst.*, 2017, pp. 2098–2104.
- [31] K. Lee, Y. Wang, and C. Zheng, "Twister hand: Underactuated robotic gripper inspired by origami twisted tower," *IEEE Trans. Robot.*, vol. 36, no. 2, pp. 488–500, Apr. 2020.
- [32] Z. Zhang et al., "Active mechanical haptics with high-fidelity perceptions for immersive virtual reality," *Nature Mach. Intell.*, vol. 5, no. 6, pp. 643–655, 2023.
- [33] L. Paez, G. Agarwal, and J. Paik, "Design and analysis of a soft pneumatic actuator with origami shell reinforcement," *Soft Robot.*, vol. 3, no. 3, pp. 109–119, 2016.
- [34] R. V. Martinez, C. R. Fish, X. Chen, and G. M. Whitesides, "Elastomeric origami: Programmable paper-elastomer composites as pneumatic actuators," *Adv. Funct. Mater.*, vol. 22, no. 7, pp. 1376–1384, 2012.
- [35] Z. Zhang, G. Chen, H. Wu, L. Kong, and H. Wang, "A pneumatic/cable-driven hybrid linear actuator with combined structure of origami chambers and deployable mechanism," *IEEE Robot. Automat. Lett.*, vol. 5, no. 2, pp. 3564–3571, Apr. 2020.
- [36] Z. Zhang, W. Fan, G. Chen, J. Luo, Q. Lu, and H. Wang, "A 3D printable origami vacuum pneumatic artificial muscle with fast and powerful motion," in *Proc. IEEE 4th Int. Conf. Soft Robot.*, 2021, pp. 551–554.
- [37] C. Zhang et al., "Plug & play origami modules with all-purpose deformation modes," *Nature Commun.*, vol. 14, no. 1, 2023, Art. no. 4329.
- [38] J. Yi et al., "Customizable three-dimensional-printed origami soft robotic joint with effective behavior shaping for safe interactions," *IEEE Trans. Robot.*, vol. 35, no. 1, pp. 114–123, Feb. 2019.
- [39] F. Schmitt, O. Piccin, B. Bayle, P. Renaud, and L. Barbé, "Inverted honeycomb cell as a reinforcement structure for building soft pneumatic linear actuators," *J. Mechanisms Robot.*, vol. 13, no. 1, 2020, Art. no. 011020.
- [40] S. Li, D. M. Vogt, D. Rus, and R. J. Wood, "Fluid-driven origami-inspired artificial muscles," *Proc. Nat. Acad. Sci.*, vol. 114, no. 50, pp. 13132–13137, 2017.
- [41] J.-G. Lee and H. Rodrigue, "Origami-based vacuum pneumatic artificial muscles with large contraction ratios," *Soft Robot.*, vol. 6, no. 1, pp. 109–117, 2019.
- [42] J. Chen, B. Chen, K. Han, W. Tang, and Z. L. Wang, "A triboelectric nanogenerator as a self-powered sensor for a soft-rigid hybrid actuator," *Adv. Mater. Technol.*, vol. 4, no. 9, 2019, Art. no. 1900337.
- [43] A. Lotfiani, H. Zhao, Z. Shao, and X. Yi, "Torsional stiffness improvement of a soft pneumatic finger using embedded skeleton," *J. Mechanisms Robot.*, vol. 12, no. 1, 2019, Art. no. 011016.
- [44] Z. Wu, X. Li, and Z. Guo, "A novel pneumatic soft gripper with a jointed endoskeleton structure," *Chin. J. Mech. Eng.*, vol. 32, no. 1, 2019, Art. no. 78.
- [45] M. Al-Rubaiai, T. Pinto, C. Qian, and X. Tan, "Soft actuators with stiffness and shape modulation using 3D-printed conductive polylactic acid material," *Soft Robot.*, vol. 6, no. 3, pp. 318–332, 2019.
- [46] J. Zhang et al., "A survey on design, actuation, modeling, and control of continuum robot," *Cyborg Bionic Syst.*, vol. 2022, 2022, Art. no. 9754697.
- [47] G. Chen, Z. Zhang, and H. Wang, "A general approach to the large deflection problems of spatial flexible rods using principal axes decomposition of compliance matrices," *J. Mechanisms Robot.*, vol. 10, no. 3, 2018, Art. no. 031012.
- [48] G. Chen, Z. Zhang, L. Kong, and H. Wang, "Analysis and validation of a flexible planar two degrees-of-freedom parallel manipulator with structural passive compliance," *J. Mechanisms Robot.*, vol. 12, no. 1, 2019, Art. no. 011011.
- [49] M. E. Bitterman, "Vertebrate-invertebrate comparisons," in *Intelligence and Evolutionary Biology*, H. J. Jerison and I. Jerison Eds., Berlin, Germany: Springer, 1988, pp. 251–276.
- [50] H. Lu et al., "A bioinspired multilegged soft millirobot that functions in both dry and wet conditions," *Nature Commun.*, vol. 9, no. 1, 2018, Art. no. 3944.
- [51] M. Manti, V. Cacucciolo, and M. Cianchetti, "Stiffening in soft robotics: A review of the state of the art," *IEEE Robot. Automat. Mag.*, vol. 23, no. 3, pp. 93–106, Sep. 2016.
- [52] J. Rivera et al., "Toughening mechanisms of the elytra of the diabolical ironclad beetle," *Nature*, vol. 586, no. 7830, pp. 543–548, 2020.
- [53] L. Paez, M. Granados, and K. Melo, "Conceptual design of a modular snake origami robot," in *Proc. IEEE Int. Symp. Saf., Secur., Rescue Robot.*, 2013, pp. 1–2.
- [54] M. Luo et al., "Orisnake: Design, fabrication, and experimental analysis of a 3-D origami snake robot," *IEEE Robot. Automat. Lett.*, vol. 3, no. 3, pp. 1993–1999, Jul. 2018.
- [55] Y. Kim and Y. Cha, "Soft pneumatic gripper with a tendon-driven soft origami pump," *Front. Bioeng. Biotechnol.*, vol. 8, 2020, Art. no. 461.
- [56] O. Angatkina, K. Gustafson, A. Wissa, and A. Alleyne, "Path following for the soft origami crawling robot," in *Proc. Dyn. Syst. Control Conf.*, 2019, Art. no. V003T20A009.
- [57] J. Hughes, P. Maiolino, and F. Iida, "An anthropomorphic soft skeleton hand exploiting conditional models for piano playing," *Sci. Robot.*, vol. 3, no. 25, 2018, Art. no. eaau3098.
- [58] M. A. Robertson and J. Paik, "New soft robots really suck: Vacuum-powered systems empower diverse capabilities," *Sci. Robot.*, vol. 2, 2017, Art. no. eaan6357.
- [59] M. A. Robertson, O. C. Kara, and J. Paik, "Soft pneumatic actuator-driven origami-inspired modular robotic 'pneumagami'," *Int. J. Robot. Res.*, vol. 40, no. 1, pp. 72–85, 2020.
- [60] W. McMahan, B. A. Jones, and I. D. Walker, "Design and implementation of a multi-section continuum robot: Air-octor," in *Proc. IEEE/RSJ Int. Conf. Intell. Robots Syst.*, 2005, vol. 1–4, pp. 3345–3352.
- [61] J. Zhu, M. Pu, H. Chen, Y. Xu, H. Ding, and Z. Wu, "Pneumatic and tendon actuation coupled multi-mode actuators for soft robots with broad force and speed range," *Sci. China Technol. Sci.*, vol. 65, no. 9, pp. 2156–2169, 2022.
- [62] Z. Zhang, S. Tang, W. Fan, Y. Xun, H. Wang, and G. Chen, "Design and analysis of hybrid-driven origami continuum robots with extensible and stiffness-tunable sections," *Mechanism Mach. Theory*, vol. 169, 2022, Art. no. 104607.
- [63] Y. Yoshimura, "On the mechanism of buckling of a circular cylindrical shell under axial compression," Inst. Sci. Technol., Univ. Tokyo, Bunkyo City, Tokyo, Japan, Tech. Rep. NACA-TM-1390, 1955.
- [64] H. Banerjee, N. Pusalkar, and H. Ren, "Single-motor controlled tendon-driven peristaltic soft origami robot," *J. Mechanisms Robot.*, vol. 10, no. 6, 2018, Art. no. 064501.
- [65] C. D. Onal, R. J. Wood, and D. Rus, "An origami-inspired approach to worm robots," *IEEE/ASME Trans. Mechatron.*, vol. 18, no. 2, pp. 430–438, Apr. 2013.
- [66] K. Miura and T. Tachi, "Synthesis of rigid-foldable cylindrical polyhedral," in *Proc. Symmetry, Art Sci., Int. Soc. Interdiscipl. Study Symmetry, Gmuend*, Austria, 2010, pp. 204–213.
- [67] Z. Zhang, G. Chen, W. Fan, W. Yan, L. Kong, and H. Wang, "A stiffness variable passive compliance device with reconfigurable elastic inner skeleton and origami shell," *Chin. J. Mech. Eng.*, vol. 33, no. 1, 2020, Art. no. 75.
- [68] R. D. Gregorio, "A review of the literature on the lower-mobility parallel manipulators of 3-UPU or 3-URU type," *Robotics*, vol. 9, no. 1, 2020, Art. no. 5.
- [69] V. Parenti-Castelli, R. D. Gregorio, and F. Bubani, "Workspace and optimal design of a pure translation parallel manipulator," *Meccanica*, vol. 35, no. 3, pp. 203–214, 2000.
- [70] S. Huda and Y. Takeda, "Kinematic analysis and synthesis of a 3-URU pure rotational parallel mechanism with respect to singularity and workspace," *J. Adv. Mech. Des., Syst., Manuf.*, vol. 1, no. 1, pp. 81–92, 2007.
- [71] R. M. Murray, S. S. Sastry, and Z. X. Li, *A Mathematical Introduction to Robotic Manipulation*. Boca Raton, FL, USA: CRC, 1994.
- [72] G. Chen, H. Wang, and Z. Lin, "Determination of the identifiable parameters in robot calibration based on the POE formula," *IEEE Trans. Robot.*, vol. 30, no. 5, pp. 1066–1077, Oct. 2014.
- [73] S. I. Rich, R. J. Wood, and C. Majidi, "Untethered soft robotics," *Nature Electron.*, vol. 1, no. 2, pp. 102–112, 2018.
- [74] V. Cacucciolo, J. Shintake, Y. Kuwajima, S. Maeda, D. Floreano, and H. Shea, "Stretchable pumps for soft machines," *Nature*, vol. 572, no. 7770, pp. 516–519, 2019.

- [75] D. Drotman, S. Jadhav, D. Sharp, C. Chan, and M. T. Tolley, "Electronics-free pneumatic circuits for controlling soft-legged robots," *Sci. Robot.*, vol. 6, no. 51, 2021, Art. no. aay2627.
- [76] T. Ranzani, G. Gerboni, M. Cianchetti, and A. Menciassi, "A bioinspired soft manipulator for minimally invasive surgery," *Bioinspiration Biomimetics*, vol. 10, no. 3, 2015, Art. no. 035008.



**Zhuang Zhang** (Member, IEEE) received the B.S. degree in mechanical engineering from Northeastern University, Shenyang, China, in 2015, and the Ph.D. degree in mechanical engineering from Shanghai Jiao Tong University, Shanghai, China, in 2021.

He is currently a Postdoctoral Research Fellow with the School of Engineering, Westlake University, Hangzhou, China. He is the author of more than 20 academic papers published in multidisciplinary/robotics journals and conferences, including *Nature Machine Intelligence*, *Nature Communications*,

*Science Advances*, and IEEE International Conference on Intelligent Robots and Systems. His research interests include origami robots, soft-rigid hybrid robots, mechanism design, and haptics.



**Genliang Chen** (Member, IEEE) received the B.S. and Ph.D. degrees both in mechanical engineering from Shanghai Jiao Tong University (SJTU), Shanghai, China, in 2006 and 2014, respectively.

From 2016 to 2017, he was with the Biomimetic and Dexterous Manipulation Laboratory, Stanford University, as a Visiting Scholar. He is currently a Professor with the META Robotics Institute, and the State Key Laboratory of Mechanical System and Vibration, SJTU. His research interests include the mechanism design, robot kinematics, and dynamics.



**Yuanhao Xun** received the B.S. degree in mechanical engineering from Central South University, Changsha, China, in 2019. He is currently working toward the M.S. degree in mechanical engineering with the Shanghai key Laboratory of Digital Manufacturing for Thin-walled Structures, Shanghai Jiao Tong University, Shanghai, China.

His research interests include stretchable sensors, embedded system, and mechanism design.



**Yongzhou Long** received the B.S. degree in mechanical engineering from Chongqing University, Chongqing, China, in 2020. He is currently working toward the Ph.D. degree in mechanical engineering with Shanghai Jiao Tong University, Shanghai, China.

His research interests include the rigid-soft hybrid robots, bioinspired robots, and mechanism design.



**Jue Wang** (Student Member, IEEE) received the B.S. degree in mechanical engineering from the Dalian University of Technology, Dalian, China, in 2017, and the M.S. degree in mechanical engineering from Shanghai Jiao Tong University, Shanghai, China, in 2020. He is currently working toward the Ph.D. degree in mechanical engineering with the School of Mechanical Engineering, Purdue University, West Lafayette, IN, USA.

His research interests include the mechanism and robotics, magnetic control, wearable devices, and prosthetics.



**Hao Wang** received the B.S., M.S., and Ph.D. degrees in mechanical engineering from Tianjin University, Tianjing, China, in 1996, 1999 and 2002, respectively.

He is currently a Professor with the Shanghai Key Laboratory of Digital Manufacture for Thin-walled Structures, and the State Key Laboratory of Mechanical System and Vibration, Shanghai Jiao Tong University, Shanghai, China. His research interests include the mechanism design, multibody system dynamics, and smart manufacturing.



**Jorge Angeles** (Fellow, IEEE) received the Electromechanical Engineer degree and the M.Eng. degree in mechanical engineering from the National Autonomous University of Mexico, Mexico City, Mexico, in 1969 and 1970, respectively, and the Ph.D. degree in applied mechanics from Stanford University, Stanford, CA, USA, in 1973.

He is currently a James McGill Professor Emeritus with the Department of Mechanical Engineering, McGill University, Montreal, QC, Canada, and a Founding Member, then Acting Director (1996–

1997), with the Centre for Intelligent Machines, where he founded the Robotic Mechanical Systems Laboratory. He is the author or co-author of various books on kinematics and dynamics of mechanical systems plus numerous technical papers in research journals and conference proceedings.

Dr. Angeles is a Fellow of the Royal Society of Canada, the Canadian Academy of Engineers, the Canadian Society of Mechanical Engineers, and American Society of Mechanical Engineers. He is one of the 15 Honorary Members of the International Federation for the Promotion of Mechanism and Machine Science (IFToMM).